5-2020

Integrated Hyperspectral and Geochemical Analysis of the Upper Mississippian Meramec STACK Play and Outcrop Equivalents, Anadarko Basin and Ozark Uplift, Oklahoma

David Gates
University of Arkansas, Fayetteville

Integrated Hyperspectral and Geochemical Analysis of the Upper Mississippian Meramec STACK Play and Outcrop Equivalents, Anadarko Basin and Ozark Uplift, Oklahoma

A thesis submitted in partial fulfillment
of the requirements for the degree of
Master of Science in Geology

by

David Gates
Wheaton College
Bachelor of Science in Geology, 2018

May 2020
University of Arkansas

This thesis is approved for recommendation to the Graduate Council.

_____
Glenn R. Sharman, Ph.D.
Thesis Advisor

_____
Walter L. Manger, Ph.D.
Committee Member

_____
Jason A. Tullis, Ph.D.
Committee Member

_____
David F. Wheatley, Ph.D.
Committee Member

Abstract

The principle goal of this project was to investigate compositional, textural, and sedimentological variability in the Oklahoma STACK Play's Meramec Formation and time equivalent outcrops of the Pryor Creek Formation in northeastern Oklahoma and to assess the potential of a partial-SWIR (Short Wave Infrared, 900-1700 nm) hyperspectral imaging sensor for drill core and sUAS-based (small Unmanned Aircraft Systems) outcrop characterization.

The STACK Play is a colloquial term that refers to stacked unconventional petroleum reservoirs that are primarily located in Canadian, Kingfisher, Blaine, and Dewey Counties, central Oklahoma. Discovery of, and commercial production from, the play was initiated in 2011 by Newfield Exploration Co. and today comprises a significant share of unconventional petroleum production in Oklahoma. The most prolific reservoir within the STACK Play is the Meramec Formation which is approximately Meramecian in age.

Chapter 2 focuses on two drill cores from the producing Meramec Formation in Dewey and Canadian Counties of central Oklahoma. Conventional core analysis techniques, including analysis of core sedimentology, mineralogy, and geochemistry, are integrated with lab-based partial-SWIR hyperspectral analysis of both cores. The Meramec Formation comprises proximal and distal ramp deposits that include argillaceous quartz siltstones, calcareous quartz siltstones and sandstones, and lesser grainstones. Analysis of partial-SWIR hyperspectral imaging data establishes a relationship between reflectance and primary mineralogy in both cores, which was ultimately used in conjunction with other conventional core data to distinguish multiple orders of stratigraphic cyclicity in the Meramec Formation, including cyclicity that is below the resolution of typical core logging and sampling procedures.

Chapter 3 details the study of outcrops located in Pryor Quarry (Mayes County, northeast Oklahoma), which are approximately age equivalent to the Meramec Formation. The potential of sUAS-based partial-SWIR hyperspectral imaging for outcrop analysis is evaluated using lab-based full-SWIR point spectral analysis of samples taken from a vertical outcrop transect in the quarry. Outcrops of the Meramecian Pryor Creek Formation are comprised of wackestones, mudstones, quartz siltstones and to a lesser extent (<10%) packstones and grainstones. Although efforts to collect data using the sUAS-based partial-SWIR sensor were ultimately unsuccessful due to technical challenges and equipment failure, results suggest that attempting to classify outcrop composition using the partial-SWIR may be challenged by the inability to normalize incident intensity values on an outcrop face in a field setting. Recommendations are provided for the future application of sUAS-based partial-SWIR hyperspectral imaging of outcrops.

Acknowledgements

I gratefully acknowledge Bill Coffey for providing the inspiration for this project, Dave Hull for continued support and critical feedback, and Devon Energy and The American Association of Petroleum Geologists Grants-in-Aid program through which this research was funded. I am grateful to Cory Godwin for his assistance in orienting me to the local Mississippian stratigraphy and for providing the geological groundwork which contributed greatly to the inception of this thesis. Thanks to Malcolm Williamson for his good humor, technical understanding, and consistency throughout some of the most trying aspects of this project. Our car rides to Oklahoma were among some of the most memorable and thought-provoking conversations I had in all of graduate school. In addition I'd like to thank Josh Blackstock for a steady stream of innovative ideas, enthusiasm for my work, and encouragement; Marc Marino for his patience and expertise in explaining the use of pXRF equipment; Matt Covington for teaching an exceptional course, which ultimately guided my professional aspirations; Richard Coffman for lending me access to his spectroscopy equipment; Amy Gottberg for assisting me in field work; members of CAST including Adam Barnes for their technical assistance; the staff at OPIC for facilitating my description of drill cores; the Colbert family for access to Stillwell Quarry; the staff at APAC and Buzzi Unicem for allowing me to conduct field work on their property as well as many members of the University of Arkansas including, faculty and students whom without the support and guidance of I might not have come this far.

I especially would like to acknowledge the importance of each of my committee members and their contribution to my research and growth. David Wheatley provided invaluable professional guidance and perspective on a career in geoscience, Jason Tullis was a consistent

source of encouragement and remote sensing expertise, and Walt Manger provided careful editing and bottomless understanding of regional stratigraphic complexities.

Lastly, I'd like to extend my sincere gratitude to my adviser Glenn Sharman. For the last 2 years, Glenn has been a consistent source of challenge and scientific growth for me. I feel fortunate to be among Glenn's first few students at Arkansas, and I look forward to seeing the countless others who will benefit from his mentorship as I have.

Table of Contents

Chapter 1

Introduction

Meramecian strata of the Anadarko Basin and the adjacent Ozark Uplift were deposited in proximal to distal shelf environments along an east-west striking paleo-shoreline (Curtis and Champlin, 1959). Today, Meramecian strata are preserved within the subsurface of the Anadarko Basin (informally named the Meramec Formation; (Price et al., 2020)) and exposed in northeastern Oklahoma along the flanks of the Ozark Uplift in the Pryor Creek Formation (Godwin, 2017; Miller, 2018; Price et al., 2020). In the Anadarko Basin, knowledge of the Meramec Formation is largely derived from seismic and well data, including geophysical logs and drill core (Price et al., 2020). In northeastern Oklahoma, quarries provide the best exposures of the Pryor Creek Formation, where large shallow pits are excavated to acquire rock for use as aggregate in cement production (Shelley, 2016; Godwin, 2017). Although approximately 250 km separate the Meramec Formation of the STACK Play and exposures of the Pryor Creek Formation in the northeastern portion of the state, these outcrops provide an opportunity to study vertical and lateral lithologic variability in an approximately analogous geologic setting. Study of outcrops has the advantage of allowing detailed observations of lateral facies relationships that cannot be easily ascertained using widely spaced, one-dimensional, well control points. Ultimately, subsurface-to-outcrop studies may lend valuable insights into subsurface characteristics of the reservoir, which would otherwise not be discernable from subsurface datasets alone.

This research was motivated by the increasing scientific and economic interest in hyperspectral imaging for mm- to cm-scale compositional reconstruction (de Linaje et al., 2018; Cecilia Contreras Acosta et al., 2019; Jacq et al., 2019; Sun et al., 2019) This research used a

partial-SWIR hyperspectral sensor (900-1700 nm) to analyze both drill core and outcrop of Upper Mississippian strata, with a focus on the Meramecian interval. Hyperspectral sensors have traditionally been employed by satellites, aircraft, balloons, ground-based systems, and more recently small unmanned aircraft systems (sUAS) to image the non-visible portions of the electromagnetic spectrum of a given scene, ultimately for the purpose of compositional classification and endmember analysis (Okyay et al., 2016; Adão et al., 2017; Sun et al., 2017; Kirsch et al., 2018; Mohamed et al., 2018). Past researchers have leveraged the technology to accurately map mineralogy on scales ranging from square kilometers to millimeters (Notesco et al., 2015; Bachri et al., 2019; Lorenz et al., 2019). A partial-SWIR hyperspectral sensor was used in this study due to technological and cost limitations with mounting a full-SWIR sensor (1000-2500 nm) on a sUAS.

Chapter 2 examines two drill cores from the subsurface STACK Play using conventional descriptive and analytical techniques including thin section petrography, portable X-ray fluorescence (pXRF), and X-ray diffraction (XRD) in addition to hyperspectral imaging. A workflow is presented for integrating geochemical, mineralogic, sedimentologic, and hyperspectral data that includes data analysis in ENVI and Python 3. The results of Chapter 2 demonstrate that the Meramec Formation comprises autocyclic and allocyclic proximal and distal ramp deposits that range from argillaceous quartz siltstones to calcareous quartz siltstones and sandstones. Lab-based hyperspectral imaging documents five orders of cyclicity, two of which exist below the resolution captured by gamma ray log and other traditional core data.

Chapter 3 assesses the potential of sUAS-based partial-SWIR hyperspectral imaging for characterization of Meramecian and Chesterian outcrops in Pryor Quarry, Mayes County, Oklahoma. For the purposes of ground-truthing the results of the sUAS-based hyperspectral

imaging survey of Pryor quarry, an outcrop transect was described and sampled for pXRF analysis. Point-based full-SWIR hyperspectral data were collected from samples gathered from this transect from both weathered and unweathered surfaces. Although efforts to collect hyperspectral imaging data using the sUAS-based partial-SWIR sensor were ultimately unsuccessful due to technical challenges and equipment failure, results from Chapter 3 suggest that attempting to classify outcrop composition using partial-SWIR data may be challenged by the inability to control incident intensity values on an outcrop face in a field setting.

Chapter 2

Integrated Hyperspectral and Geochemical Analysis of the STACK Play

Abstract

The study of drill core allows for the quantification of primary compositional, textural, and sedimentological controls on reservoir properties. However, conventional core analysis techniques are often time consuming, and in some cases, destructive and of limited spatial resolution. High-resolution partial-Short Wave Infrared (partial-SWIR, 900-1700 nm) hyperspectral imaging (HI) was conducted on two Mississippian drill cores from the central Oklahoma STACK Play (Sooner Trend, Anadarko Basin, Canadian and Kingfisher Counties) at a spatial resolution of ~1.5mm. Unsupervised classifications were used to identify eight spectral classes in each core. Conventional portable X-ray fluorescence (pXRF), X-ray diffraction (XRD), and sedimentologic data were used to assess whether these partial-SWIR spectral classes possess any distinct compositional (elemental geochemical and mineralogic) and/or sedimentological characteristics. Additionally, detailed sedimentologic descriptions of the Meramecian core were used to define lithofacies as a basis for integration with HI data.

Results indicate that variation in reflectance values in the partial-SWIR range (900-1700 nm) are driven by the abundance of three primary mineralogical end members, calcite, quartz, and clay. Spectral classes are shown to be sensitive to mineralogy, and by extension elemental geochemistry, with low reflectance classes having a high quartz and clay (Si and Al) content, and high reflectance classes having a high calcite (Ca) content. The relationship between spectral class and mineralogy, and the continuous and high-resolution nature of HI data, allows for the quantification of mineralogy, geochemistry, and depositional cyclicity of the STACK cores at a much finer spatial resolution than possible with conventional descriptive methods.

1. Introduction

The rough surface texture on a rock or mineral causes incident light to be scattered at many angles in a process known as diffuse reflection (van der Meer, 2004). Reflection can be measured as the proportion of diffusely reflected energy relative to the total amount of energy incident on a surface and is typically expressed as a percentage (Coakley, 2003). The proportions of incident energy that are either reflected, absorbed, or transmitted are a function of the angular distribution of incident energy, the unique compositional and textural characteristics of the material, and the wavelength of the incident energy (Coakley, 2003; Kirsch et al., 2018). It should be noted that the proportion of reflected light is not intrinsic to a material, but rather the result of a complex interplay between variables concerning both incident energy and the properties of a material (Sun et al., 2019). If variability in the intensity and angular distributions of incident energy can be controlled in a lab setting, however, then in theory the compositional and textural parameters of the material can be studied (Jakob et al., 2017; Greene et al., 2019)

Reflectance information is typically recorded as a function of wavelength at the spectral resolution of the sensor. These data are most efficiently visualized as a unique 2D plot of reflectance vs wavelength for each pixel in the image called a spectral signature (Kurz et al., 2012; Gewali et al., 2018). The spectral signature can be divided into two meaningful components, (1) the continuum, which describes the general character of the spectral curve as reflectance varies from band to band, and (2) absorption features that occur where certain molecules absorb energy at specific wavelengths through electronic or vibrational processes (Zaini et al., 2014; de Linaje et al., 2018; Mohamed et al., 2018; Sun et al., 2019). When present, absorption features are typically manifested as steep troughs in the spectral signature (van Ruitenbeek et al., 2006).

Conventional means of classifying hyperspectral images in the Visible and Near-Infrared (VNIR, 400-1000 nm) and full-Short Wave Infrared (full-SWIR, 1000-2500 nm) have traditionally relied on identifying absorption features diagnostic of specific minerals and quantifying the variability in their position and geometry to better understand relative abundance, grain size, and crystal structure (Cooper and Mustard, 1999; Zaini et al., 2012). While many studies have utilized this method to reliably reconstruct common sedimentary mineralogy at cm-scale spatial resolution, the spectral range necessary to do so typically demands sampling from both the full-SWIR and the Long-Wave-Infrared (LWIR, 8000-12000 nm), which requires multiple sensors (Zaini et al., 2014; Kirsch et al., 2018; Cecilia Contreras Acosta et al., 2019; Jacq et al., 2019). These sensors are not only expensive, but can be quite large and heavy to accommodate cooling systems necessary to image portions of the infrared spectrum.

This study explores the utility of hyperspectral data in the partial-SWIR range (900-1700 nm) for the purpose of sedimentological analysis of drill core from a fine-grained, siliciclastic, hydrocarbon reservoir (STACK Play, Anadarko Basin, Oklahoma). Because absorption features for common sedimentary minerals are in the range of 2200-2500 nm and 8000-12000 nm, studies do not generally utilize the partial-SWIR portion of the spectral response for the purpose of sedimentary rock analysis (Notesco et al., 2015; Jacq et al., 2019). In this study, unsupervised multivariate classification techniques are used on partial-SWIR HI data from drill core to demonstrate that meaningful geochemical and sedimentological information can be gleaned at mm-scale spatial resolutions, despite the lack of diagnostic mineral absorption features.

This study addressed the following research questions using slabbed drill cores from Canadian and Dewey counties in the Upper Mississippian Meramec Formation of the central Oklahoma STACK Play. (1) What lithofacies exist in the Meramec Formation and do they have

distinctive sedimentological, geochemical, and/or mineralogical properties? (2) Can Partial-SWIR HI categorize drill core on the basis of lithology, elemental geochemistry, mineralogy, and/or sedimentology?

2. Geologic Background

2.1. Structural Setting

The Anadarko Basin formed in response to failed rifting of an Early to Middle Cambrian aulacogen and subsequent thermal subsidence of the southern Oklahoma trough until the early Mississippian (Perry, 1989). Increased accommodation during thermal subsidence allowed the deposition of early to middle Paleozoic sediments, including the Upper Mississippian Meramec Formation (Johnson, 1989; Perry, 1989). Following the Mississippian, compressional and transpressional activity brought on by the collision of Gondwana and Laurentia produced the nearly contemporaneous Pennsylvanian Amarillo-Wichita and Arbuckle Uplifts, marking the transition from rift to foreland basin complete (Granath, 1989; Satterfield and Standridge, 2017). Subsidence rates then increased rapidly to accommodate Late Paleozoic sediments that comprise the bulk of the basin fill today (Ball et al., 1991).

2.2. Climatic Setting and Sea Level

The Upper Mississippian of the North American midcontinent was deposited in a subtropical climate of warm shallow seas (Gutschick and Sandberg, 1983). Paleolatitudes of the Anadarko Basin were likely 25-30º south of the equator. Significant global temperature transition from warmer conditions of the Devonian to cooler conditions of the Permian impart a strong, climatically-driven, eustatic interpretation for lower orders of observed cyclicity in the Upper Mississippian sediments in this study (Rogers, 2001; Nardin et al., 2011)

2.3. Depositional and Stratigraphic Setting

Depositional interpretations suggest that the Meramec Formation was deposited on a low relief ramp, and consisted of prograding, subaqueous clinoforms of presumed deltaic origin striking northeast-southwest (Price et al., 2020). These conditions likely extended along strike well into northeastern Oklahoma (Shelley, 2016; Godwin, 2017). The Meramec Formation pinches out to the northwest giving way to a thick succession of Mississippian platform carbonates buried at shallow depths and covering thousands of square km, known as the Burlington Shelf (Gutschick and Sandberg, 1983). To the southeast, the Meramec Formation thickens before pinching out again in this direction. Today, the Arbuckle Uplift defines the southern margin of the basin and exposes deep-water sediments of the Meramecian Sycamore Formation (Coffey, 2001). The Sycamore Formation is interpreted as a series of distal basin deposits punctuated by sediment gravity flows, namely turbidites, that comprise the exhumed Meramecian depocenter of the Anadarko Basin (Perry, 1989; Coffey, 2001).

2.4. STACK Play

The STACK Play is a colloquial term referring to the supergroup of stacked, unconventional, hydrocarbon reservoirs located in the Anadarko Basin of central Oklahoma (Price et al., 2020). The informally named ‘Meramec Formation’ constitutes the productive heart of the play overlying the fracture-dominated, Osage Limestone and the Woodford Shale regional source rock, and underlying the regionally extensive and competent cap rock of the Chester shale (Price et al., 2020). Although a general understanding of the stratigraphy places the Meramec Formation in the Late Mississippian, subsurface biostratigraphic data is not publicly available for establishing age constraints on the informally designated formations of the Osage, Meramec, and

Chester. For this reason, in this study, these formation names are used as pseudo-lithostratigraphic, and not biostratigraphic, units (Godwin, 2017; Miller, 2018).

The Meramec Formation has been described in previous studies as a fine-grained, predominantly quartz siltstone with smaller fractions of clay and scattered calcite cement (Shelley, 2016; Miller, 2018) The Meramec Formation's commercial productivity centers around Canadian, Kingfisher, and Blaine Counties, and smaller portions of Dewey, Woodward, Major, and Garfield Counties (Hardwick, 2018; Miller, 2018) (Fig. 1).

3. Methods

Two drill cores from Canadian and Dewey Counties were examined in this study. Hyperspectral images, pXRF measurements, and measured sections were collected from these cores at the Oklahoma Geological Survey in Norman, Oklahoma. In addition, this study includes analysis of X-ray diffraction (XRD) data, core photographs, and thin sections provided by Devon Energy (Table 1).

Table 1. Overview of Datasets Used for this Study.

	Collected Data			***Devon Energy Data***		
	Hyperspectral images	*pXRF*	*Lithofacies descriptions*	*XRD*	*Thin sections*	*RGB photos*
Dewey County core	***X***	***X***	***X***		***X***	***X***
Canadian County core	***X***	***X***	***X***	***X***	***X***	***X***

Abbreviations: pXRF – portable X-ray fluorescence; XRD – X-ray diffraction

3.1. Partial-SWIR Hyperspectral Imaging (BaySpec OCI-F Hyperspectral Sensor)

3.1.1. Data Collection

Core hyperspectral data were collected using the BaySpec OCI™-F hyperspectral push-broom sensor on two slabbed Meramec Formation cores from Dewey and Canadian counties at a

spatial resolution of approximately 1.5 mm (Table 2). Core scanning was performed under static lighting conditions in a laboratory setting. Four 500-Watt halogen lightbulbs were mounted on tripods and placed symmetrically about the scanning area (Fig. 2). Because intensity varies as a function of the inverse square distance between the light source and the surface of the core, care was taken to ensure that the lighting apparatus was constructed geometrically about the scanning area to provide near uniform values of incident intensity on the full surface of the core. This step was necessary because the empirical line calibration technique used in this study to convert raw intensity data to reflectance values requires the use of a linear interpolation between dark and white references of known reflectivity.

Prior to hyperspectral imaging, all core surfaces were cleaned of dust and debris using water and paper towels. Cores were then dried fully before scanning. The hyperspectral sensor was mounted to a tripod 0.9 m above the tabletop scanning area. BaySpec proprietary acquisition software SpecGrabber was used to remotely control the hyperspectral sensor and initiate raw image capture of the core boxes . Each core box measured 0.6 by 0.45 m and contained five, 0.6 m segments of slabbed core. Up to seven core boxes at a time were placed end-to-end oriented on the longer dimension, and steadily guided on the roller top table under the push-broom sensor to be recorded within a single scanning run (Fig. 2). Imaging times lasted approximately two minutes for each set of seven boxes. This process was repeated in sets of seven until all core boxes from both cores were scanned. A total of 83.2 and 36.6 m of core were scanned for the Canadian and Dewey County cores respectively.

Table 2. BaySpec OCI-F Hyperspectral Sensor Specifications as given by BaySpec, Inc

Operation Mode	*Push-broom*
Spectral Range	*900-1700 nm*
Spectral Resolution	*10 nm*
Spectral Bands	*80*
Spatial Pixels	*250 pixels X scan-length*
Weight	*820 grams*
Sensor Dimensions	*17 x 7 x 9 cm*
Field of View (FOV)	*28°*

3.1.2. Pre- and Post-Processing

Pre-processing of raw image data into hyperspectral image (HI) cubes was completed using BaySpec proprietary software CubeCreator. Output HI cubes contained 72 bands across a range of 960-1680 nm. Bands inside the 900-960 nm and 1680-1700 nm range are characterized by a low signal-to-noise ratio and were filtered out in the data collection phase. Post-processing of the HI cubes involved using ENVI image processing software to mosaic HI cubes from separate imaging runs as well as masking non-rock features. Forward minimum noise fraction (MNF) transforms were then conducted on the mosaic HI cubes for both the Canadian and Dewey County cores to segregate noise in the data, producing an output of 72 components. Calculated eigen values were then used to determine which components maximized variance (*i.e.*, signal bearing) and by effect possessed, minimal noise. The first seven and nine components for the Canadian and Dewey County cores, respectively, were determined to account for 95% of the total variance in the data. This subset of meaningful components for each core was then used for classification.

3.1.3. Classification

Preliminary core classification was computed using the unsupervised algorithm ISODATA (Iterative Self-Organizing Data Analysis Techniques). Since the spectral range of the

hyperspectral sensor is not inclusive for absorption features typical of common sedimentary minerals, it was important to use the unsupervised approach so classifications could be calculated using data from the full spectral range of the hyperspectral sensor. Initially, 20 classes for both cores were computed, then the classes were superimposed as false color images on band 1 of the HI cube and examined closely. Classes that appeared to represent spectral artifacts or shadows were masked-out. Some classes were merged, where obvious spatial relationships and knowledge of the underlying geology made it reasonable to do so. In total, 8 classes were retained for each core and determined to represent true variation in the underlying geology.

3.2. Portable X-ray Fluorescence Analysis (Olympus Vanta M Series pXRF Analyzer)

3.2.1. Sampling Procedure

Discrete pXRF geochemical analyses were performed on both cores to map elemental abundances at a minimum resolution of one foot. Additional measurements were taken on areas of the core, where visually distinct changes in lithology occurred. To account for instrument drift, Montana Soil Standard SRM 2711a was measured at the start and end of each day of sampling. If abundances of the primary elements present in the standard drifted from known laboratory values by more than 10%, the film over the instrument beam was cleaned, the settings were checked, and the process repeated until the instrument achieved results within the acceptable margin of error. A total of 222 and 127 measurements were taken on the Canadian and Dewey County cores, respectively.

3.2.2. Matrix Correction

Fundamental parameters are the established factory method of calibrating pXRF instruments, routed in the theoretical relationship between measured X-ray intensities and the concentrations of elements in the sample (Chawchai et al., 2016). While this calibration method

produces a robust qualitative tool, it does not properly account for the variance introduced by matrix effects in a given rock sample. For this reason, it is best to establish linear matrix correction models using sedimentary rock standards with similar composition and crystalline structure to the lithofacies types being studied.

In this study, four sedimentary standards with lab verified ICP-MS elemental abundance values were used: two argillaceous limestones and two quartz siltstones. Although agreement between reported and measured values for both elements is strong, suggesting that matrix effects are minimal, linear interpolation models were constructed for both Si and Ca and used to correct raw pXRF data (Fig. 3)

3.3. Core Descriptions and Lithofacies Interpretation

Core descriptions were conducted taking note of sedimentary structures, bedding thickness, and lithology at the dm scale. Thin section samples were previously collected by Devon Energy and were stained with alizarin red S for calcite identification and injected with blue epoxy to identify porosity. A Leica DM 2700P microscope was used to observe the thin sections in plane-polarized and cross-polarized light. Thin sections were analyzed to quantify lithology, mineralogy, and texture. Lithofacies were defined based on a combination of detailed core descriptions, petrographic analysis of thin sections, and geochemical/mineralogical data (pXRF and XRD).

3.4. Data Analysis and Data Integration

In-house, Python scripts were developed to complete a series of sequence operations including: 1) examining the geochemical and mineralogic properties of each lithofacies, 2) visualizing the distribution of spectral classes on the core, 3) calculating and plotting confidence intervals for each spectral class, 4) depth referencing and normalizing spectral class abundances

of the core, 5) indexing and examining the geochemical and mineralogic properties of each spectral class, 6) identifying the relationship between lithofacies and spectral classes, 7) identifying sedimentary cyclicity using spectral class data, and 8) integrating classification data with pXRF, XRD, lithofacies classification, and RGB photographs in comparative subplots.

4. Results

4.1. Mineralogy and Elemental Geochemistry

4.1.1. Canadian County Core

XRD data indicate that the Meramec Formation in the Canadian County core is primarily comprised of quartz (17-59%), calcite (2-78%), clay (2-41%), plagioclase feldspar (2-11%), and potassium feldspar (1-9%) (Table 3). Dolomite in this core is rare, but when present, occurs in beds of <0.2 m at high concentrations (1-35%). Additional minerals present in trace (<5%) amounts include, muscovite, pyrite, marcasite, and apatite.

pXRF data indicate that light elements (Na and lower atomic numbers, including O) comprise 53-60% of the core. The remainder of the core is composed of Si (5.2-37%), Ca (0.8-35%), and Al (0.3-7.6%). Additional elements, including Mg, K, Fe, P, and S, are present in trace abundances (<5%).

The abundance of calcite and/or Ca in both cores reflects the equal parts of interparticle calcite cementation and detrital carbonate largely in the form of peloids. Samples with high calcite, and Ca content mostly consist of clean (clay-poor), light gray lithologies that are also relatively poor in Al. Conversely, lithologies with a higher proportion of dark, argillaceous matrix are clay rich and, according to Price et al. (2020), possess the highest porosity and permeability within the Meramec Formation. Confidence intervals for pXRF and XRD data

indicate that lithofacies share significant compositional overlap, but generally exist on a dual endmember spectrum, where quartz and clay-rich lithofacies oppose calcium-rich lithofacies (Figs. 4 and 5).

4.1.2. Dewey County Core

Quantitative mineralogical data (XRD) were not collected for the Meramec Formation in the Dewey County core. However, qualitative estimations of primary mineralogy from thin section suggest a similar mineral assemblage as in the Canadian County core, although the lower third of the core exhibits a greater abundance of primary detrital calcite grains and lesser clay. Confidence intervals for pXRF data indicate that while lithologies in the Dewey County core possess some compositional overlap, they plot in more distinctive groupings than lithologies of the Canadian County core (Fig. 6).

pXRF data indicate that light elements comprise 52-62% of the core. The remainder of the core comprises Si (0.6-33.2%), Ca (1.0-39.8%), and Al (0-10.6%). Additional elements, including Mg, K, Fe, P, and S, are present in trace abundances (<5%).

4.2. Sedimentology, Lithofacies, and Stratigraphic Setting

4.2.1. Canadian County Core

The Canadian County core includes the upper 3 m of the Osage Formation and 80.2 m of the Meramec Formation (extending into the middle portion of this formation). At the base of the Canadian County core, the Osage Formation is predominantly a lightly burrowed, massive, light gray, calcareous peloidal siltstone with scattered clasts of dark micrite, and a few preserved cm-sized, white fossil fragments. Vertical fractures are common and healed with calcite. The Meramec Formation is generally described as a dark grey to brown, calcareous to argillaceous, quartz siltstone with varying levels of calcite cement, localized intense burrowing and/or mm-

scale planar laminations. Meter to several meter packages of amalgamated, light grey, massively bedded, calcite-cemented quartz siltstones and sandstones with sharp erosive bases occur intermittently throughout the core. The Canadian County core was classified into seven lithofacies based on distinctive compositional (mineralogical and geochemical), and sedimentologic characteristics (grain size, bedding thickness, and sedimentary structures).

Lithofacies 1 – Graded, burrowed, argillaceous quartz siltstone and mudstone

Lithofacies 1 accounts for 25% of the Canadian County core and is comprised of stacked 0.5-1.5 m fining-upwards sequences that can be broken into three subunits: 1) burrowed, medium gray, argillaceous, quartz siltstones that grade into 2) dark gray, planar-laminated, argillaceous, quartz siltstones that grade into 3) sub-mm scale, planar-laminated, black, clay-rich mudstones (Fig. 7). The dark grey, planar-laminated, quartz siltstone of subunit 2 is compositionally and sedimentologically identical to lithofacies 2, but possesses a genetic gradational relationship with subunits one and three that distinguishes it as part of a separately defined lithofacies. The fabric of subunit 2 consists of medium quartz silt and a clay matrix (Fig. 8). The darker grey color of the planar-laminated and burrowed siltstones reflects a high clay content (average of 29%) (Table 3). Correspondingly, this lithofacies exhibits a general lack of calcite and feldspar (average of 13% and 15% respectively), and an abundance of quartz (average of 42%) (Table 3). The average elemental geochemistry of lithofacies 1 is Si (27%), Ca (9%), and Al (4%) (Table 3).

Lithofacies 2 – Argillaceous quartz siltstone

Lithofacies 2 is an argillaceous, quartz siltstone that comprises 9% of the Canadian County core. This lithofacies is dull grey to brown in color, characterized by faint, mm-scale,

planar laminations with rare 2-5 cm, upwards-fining packages and lacks bioturbation (Fig. 7). Lithofacies 2 is dominantly comprised of silicates quartz, feldspar, and clay (45%, 14%, and 23% on average, respectively) with a lesser abundance of calcite (15% average), which is primarily present as cement (Table 3). Quartz grains are predominantly sub-angular, and organic content is visually estimated in thin section to be approximately 15% by volume (Fig. 8). Minor phosphatic sands can be observed in hand specimen and thin section. Si, Ca, and Al content are similar to lithofacies 1: averages of 30%, 6%, and 5%, respectively.

Lithofacies 3 – Calcareous, bioturbated quartz siltstone

Lithofacies 3 accounts for 14% of the Canadian County core and occurs almost exclusively in the basal third of that core. Lithofacies 3 is a medium gray, calcite-cemented quartz siltstone with dark brown to black, clay-filled burrows (Fig. 7). Burrowing is visible in hand specimen and is likely responsible for the poor degree of sorting observable in thin section (Fig. 8). Lithofacies 3 is distinguishable from lithofacies 1 on the basis of the increased presence of calcite cement (35% average), and the decreased presence of clays (18% average). Quartz content is comparable (38% average) to calcite cement, but feldspars have a lower average abundance (8%). While lithofacies 1 is only burrowed at the base of each sequence, lithofacies 3 is thoroughly burrowed and lacks the graded changes in grain size observable in lithofacies 1. The dominant average elements in this lithofacies are Si (23%), Ca (12%), and Al (4%).

Lithofacies 4 – Graded, calcareous, quartz siltstone and sandstone that is interbedded with bioturbated, argillaceous quartz siltstone

Lithofacies 4 composes many stacked, graded, 3-15 cm fining-upwards sequences totaling 10% of the Canadian County core. The base of each sequence is typically a light gray,

clean, calcite-cemented, quartz siltstone identical in composition to lithofacies 5 grading upwards into a gray, burrowed, increasingly clay-rich, calcite-cemented, quartz siltstone that is sometimes capped by a mm- to cm-thick package of dark grey to black, clay-rich mud with mm-scale planar laminations (Fig. 7). Each bed of calcareous siltstone and/or sandstone forms an erosive base with the finer beds below. Calcite-cemented, quartz siltstone at the base of each sequence is often fractured and healed with calcite. Mineralogy of lithofacies 4 is primarily calcite (average of 46%) that is predominantly an interparticle cement with framework grains of quartz and feldspar (32% and 11% average, respectively). Clay (average of 10%) is concentrated in both burrows and at the top of sequences (Fig. 8). The average elemental geochemistry of lithofacies 4 is Si (21%), Ca (17%), and Al (2%) (Table 3).

Lithofacies 5 – Calcareous quartz siltstone and very fine sandstone

Lithofacies 5 is a massive, calcite-cemented quartz siltstone and very fine sandstone with abundant silt-size peloids and a few skeletal fragments. This lithofacies accounts for 17% of the Canadian County core and is interbedded with infrequent, mm-scale, mud laminations (Fig. 7). This lithofacies is light gray, lacks bioturbation, and comprises a framework of silt to very fine-grained, sub-angular quartz and peloid grains. Lesser quantities of skeletal fragments, feldspar grains, and muscovite grains are also present. Correspondingly, quartz constitutes an average of 29% of this lithofacies (Table 3). A low clay content (4% on average) reflects the lack of an argillaceous matrix, and the relatively high calcite content (58% on average) indicating subequal parts interparticle calcite cement and peloidal silt, the former occluding most of the porosity in this facies, (Fig. 8). Feldspars make up on average an additional 9% of the detrital composition of this lithofacies. The average elemental portion of this lithofacies is Si (22%), Ca (17%), and Al (2%) (Table 3). XRD data indicate that several cm-scale beds of dolomite occur scattered

throughout lithofacies 5. Dolomite is variable in color, but typically light reddish-gray. Elemental geochemistry of dolomites reveals high Mg content (up to 5%). Dolomite constitutes less than one cumulative foot of the core.

Lithofacies 6 – Calcareous quartz siltstone and sandstone interbedded with argillaceous quartz siltstone

Lithofacies 6 accounts for 8% of the Canadian County core and includes many mm- to cm-scale beds of clean, light gray, calcareous siltstone and sandstone, interbedded with light brown, planar- to flaser-bedded, argillaceous siltstone (Fig. 7). The underlying, finer-grained, argillaceous siltstones are typically truncated by deposition of the coarser-grained calcareous siltstones and sandstones. Mineralogical makeup of lithofacies 6 is predominantly calcite (63% on average that is dominantly interparticle cement) and framework grains of quartz (25% on average) and feldspar (7% on average) (Table 3; Fig. 8). Clay (average of 5%) is present in the interbeds of light brown, argillaceous siltstone. The average elemental abundance of lithofacies 6 is Si (20%), Ca (18%), and Al (2%) (Table 3).

Lithofacies 7 – Calcareous, peloidal siltstone

Lithofacies 7, only found at the base of the Canadian County core, represents the entirety of the Osage Formation, and makes-up 7% of the core. Lithofacies 7 is gray to brown, heavily fractured, and mostly composed of peloid and quartz silt framework grains, with a minor amount of crinoid skeletal fragments (Figs. 7 and 8). Clasts of dark micrite and white shell fragments are scattered throughout this lithofacies (Fig. 7). The matrix is mostly crystalline calcite, particularly coarse, sparry calcite cement. Porosity is highly occluded by the cement. Fractures are very common and often filled with secondary calcite (Fig. 8). Compositionally, lithofacies 7 is mostly

calcite (average of 74%) as detrital peloidal grains, calcite cement, and healed secondary fractures. Smaller average fractions of quartz (18%), feldspar (7%) and clays (2%) also exist in this lithofacies (Table 3). The average elemental geochemistry of lithofacies 4 is Si (12%), Ca (26%), and Al (1%) (Table 3).

Table 3. Lithofacies summary, Canadian County core

Lithofacies	*XRD % (min/avg/max)*					*pXRF % (min/avg/max)*			*Bed Thickness*	*Sedimentary structures and notable features*	*Grain Size*
	Quartz	*K-Feldspar*	*Plagioclase*	*Calcite*	*Clays*	*Si*	*Ca*	*Al*			
LF1: Graded, burrowed, argillaceous quartz siltstone and mudstone	*28/42/59*	*1/6/9*	*6/9/11*	*2/13/35*	*19/29/41*	*13/27/37*	*1/9/23*	*1/4/8*	*0.1-1 cm*	*Graded bedding, planar bedding, burrows*	*Medium siltstone, Mudstone*
LF2: Argillaceous quartz siltstone	*32/45/53*	*4/5/6*	*6/9/11*	*8/15/20*	*10/23/33*	*25/30/33*	*4/6/9*	*3/5/6*	*1-2 mm*	*Planar laminations*	*Medium to fine siltstone*
LF3: Calcareous, bioturbated quartz siltstone	*29/38/51*	*1/3/6*	*3/5/7*	*19/35/53*	*9/18/35*	*17/23/33*	*3/12/18*	*3/4/6*	*N/A*	*Skeletal fragments, burrows*	*Medium siltstone*
LF4: Graded, calcareous quartz siltstone and sandstone that is interbedded with bioturbated, argillaceous quartz siltstone	*20/32/43*	*2/4/8*	*5/7/8*	*14/46/67*	*3/10/26*	*11/21/31*	*6/17/28*	*1/2/5*	*1-10 cm*	*graded bedding, burrows, planar laminations*	*Medium siltstone, Mudstone*
LF5: Calcareous quartz siltstone and very fine sandstone	*19/29/38*	*1/3/4*	*2/6/8*	*45/58/73*	*3/4/5*	*12/21/33*	*6/17/26*	*1/2/4*	*1-25 cm*	*Flaser bedding, massive bedding*	*Coarse siltstone, very fine sandstone*
LF6: Calcareous quartz siltstone and sandstone interbedded with argillaceous quartz siltstone	*18/25/32*	*0/2/3*	*3/5/6*	*53/63/73*	*5/5/6*	*12/20/29*	*8/18/26*	*1/2/3*	*0.1-1 cm*	*flaser bedding, planar bedding, massive bedding*	*Fine to coarse siltstone and very fine sandstone*
LF7: Calcareous, peloidal siltstone	*17/18/19*	*1/3/4*	*2/4/6*	*69/74/78*	*2/2/2*	*5/12/19*	*21/26/35*	*0/1/2*	*0.1-10 cm*	*Skeletal fragments, fractures*	*Coarse siltstone, micrite*

Abbreviations: LF – lithofacies; min – minimum; avg – average; max – maximum; mm – millimeter; cm – centimeter; m – meter

4.2.2. Dewey County Core

The Dewey County core is located up structural and depositional dip from the Canadian County core, and consequently the Meramec Formation is considerably thinner. This core includes the upper 7.6 m of the Osage Formation, the full Meramec Formation thickness (28.4 m), and 0.6 m of the overlying Chester Formation. At the base of the Dewey County core, the Osage Formation is a light gray to off white, porous, skeletal grainstone that is rich in chert clasts and stylolites. The lower half of the overlying Meramec Formation is transitional with the underlying Osage Formation and cycles between quartz- and calcite-rich intervals. The lower half of the Meramec Formation includes sequences of light gray, calcite-cemented, quartz siltstones interbedded with porous, skeletal grainstones overlain by sequences of dark gray, planar-laminated, argillaceous quartz siltstones interbedded with pure quartz siltstones. The upper half of the Meramec Formation is primarily a ripple- to planar-laminated, calcareous quartz siltstone with varying amounts of clay and bioturbation that is interspersed with occasional packages of interbedded, clean quartz siltstone and cm-bedded shales. The overlying Chester Formation is entirely a dark black, clay-rich, fissile shale.

Lithofacies 1 – Fissile shale

Lithofacies 1 is a well laminated, fissile, clay-rich, black shale with a few white, coarse skeletal fragments that occurs exclusively in the Chester Formation in the top 3% of the Dewey County core (Fig. 9). Lithofacies 1 is friablecm due to its heightened clay content. Average elemental geochemistry of lithofacies 1 indicates a high Si content (26%) with lesser Al (8%) and Ca (3%), reflecting a high clay content (Table 4).

Lithofacies 2 – Interbedded quartz siltstone and mudstone

Lithofacies 2 composes 8% of the core and is comprised of 5-25 cm beds of light to medium gray quartz siltstone overlain sharply by 0.5-3 cm packages of dark gray, clay-rich, planar-laminated mudstone (Fig. 9). Quartz siltstone beds are heterogeneous in structure and can be massive, planar-laminated, bioturbated, and/or exhibit soft sediment deformation, including dish structures. The color of the quartz siltstone is largely dependent on the degree of burrowing present and varies from light gray to black. Average elemental geochemistry of lithofacies 2 is primarily Si (28%), reflecting the abundance of detrital quartz silt observed in thin section, with lesser Ca (7%) that is likely present in minor calcite cements (Fig. 10). Thin beds of mudstone are likely responsible for the average Al content (6%).

Lithofacies 3 – Inclined- and planar-laminated quartz siltstone

Lithofacies 3 is a quartz siltstone characterized by well-developed and continuous mm-scale inclined and planar laminations that comprises the 16% of the Dewey County core (Fig. 9). Color varies on a sub-mm bed scale reflecting mineral abundance with darker and lighter intervals indicating increased clay matrix and calcite cement respectively, as visible in thin section (Fig. 10). Rare 1-2 cm burrowed intervals exist in this lithofacies that completely disrupt laminations. The average elemental abundances in this lithofacies are Si (25%), Ca (11%), and Al (4%) (Table 4).

Lithofacies 4 – Calcareous quartz siltstone and sandstone that grades to argillaceous quartz siltstone and mudstone

Lithofacies 4 is composed of many stacked 3-10 cm sequences of finely laminated, clean, light gray, calcareous quartz siltstone that grades into mottled light and dark gray, bioturbated, argillaceous quartz siltstone, and capped by black 1-10 mm beds of mudstone (Fig. 9).

Calcareous siltstones at the base of the sequence are often fractured and healed with calcite. Burrowing and mud content increase vertically in each sequence. The primary elemental abundances in this lithofacies are Si (22%), Ca (15%), and Al (3%) (Table 4).

Lithofacies 5 – Interbedded bioclastic, calcareous quartz siltstone and skeletal grainstone

Lithofacies 5 is a pale-blueish to medium gray, calcareous, locally laminated, quartz siltstone with occasional mm-scale, white gravel beds of crinoid fragments, black mud clasts, and white skeletal fragments occasionally interbedded with 5-15 cm beds of off-white, porous, skeletal grainstones identical to those in succeeding lithofacies 6 (Figs. 9 and 10). Lithofacies 5 possesses a broad range of elemental abundances with average values of Si (21%), Ca (18%), and Al (2%). Geochemical variation in this lithofacies results in concentrations of Si and Ca that range from 3-29% and 6-35%, respectively (Table 4)

Lithofacies 6 – Skeletal grainstone

Lithofacies 6 is composed of light gray to off white, coarse, porous skeletal grainstones that are rich in chert clasts and stylolites (Fig. 9). Clay is scarce in this lithofacies. Elemental geochemistry reveals that Ca accounts for 37% of this lithofacies, while Si and Al only contribute 4% and 1%, respectively (Table 4). Lithofacies 6 comprises the entirety of the Osage Formation in this core, but also occurs interbedded with lithofacies 5 in the Meramec Formation.

Table 4. Lithofacies summary, Dewey County Core.

Lithofacies	*pXRF % (min/avg/max)*			*Bed Thickness*	*Sedimentary structures and notable features*	*Grain Size*
	Si	*Ca*	*Al*			
LF1: *Fissile shale*	*24/26/29*	*1/3/5*	*6/8/11*	*<1mm*	*Planar laminations, fissile, skeletal fragments*	*Clay*
LF2: *Interbedded quartz siltstone and mudstone*	*10/28/31*	*1/7/29*	*3/6/10*	*0.1-20cm*	*Erosive base, planar laminations, soft sediment deformation features, burrows*	*Mudstone, medium siltstone*
LF3: *Inclined- and planar-laminated quartz siltstone*	*20/25/31*	*4/11/16*	*3/4/6*	*1mm*	*Ripple bedding, planar bedding*	*Coarse siltstone*
LF4: *Calcareous quartz siltstone and sandstone that grades to argillaceous quartz siltstone and mudstone*	*17/22/31*	*8/15/22*	*2/3/5*	*0.1-5 cm*	*Hummocky cross stratification, planar bedding, burrows*	*Mudstone, coarse siltstone*
LF5: *Interbedded bioclastic, calcareous quartz siltstone and skeletal grainstone*	*3/21/29*	*6/18/35*	*0/2/4*	*0.1-10 cm*	*Hummocky cross stratification, mud lenses, skeletal fragments, fractures*	*Mudstone, fine siltstone w/ bioclastic coarse sand*
LF6: *Skeletal grainstone*	*1/4/33*	*10/37/40*	*0/1/1*	*Massive*	*Stylolites, chert nodules*	*Grainstone*

Abbreviations: LF – lithofacies; min – minimum; avg – average; max – maximum; mm – millimeter; cm – centimeter; m – meter

4.3. Hyperspectral Core Classification

A total of eight spectral classes with distinctive reflectance properties were defined for each core (Figs. 11 and 12). Although spectral classes for each core share the same color scheme of increasing color warmth with increasing average reflectance, spectral classes only indicate relative changes in reflectance values for their respective core, and cannot be used to differentiate between cores. Because there are no major absorption features associated with sedimentary minerals in the 900-1700 nm spectral range, spectral classes are classified by average reflectance spectra, rather than by the geometry of any present absorption features. A weak water absorption feature at ~1440 nm associated with vibrational processes of the hydroxyl functional group O-H gives some character to the spectral signature of the unsupervised classes in both cores. This absorption feature, however, is not distinctive of cation hydroxyl bonds (i.e., Al-OH) associated with the presence of clay mineralogies, and cannot be utilized for the purpose of identifying mineralogy.

4.3.1. Mineralogy, Geochemistry, and Lithofacies Abundance of Spectral Classes

The spectral classes in both cores are characterized by distinctive mineralogy and geochemistry (Figs. 13 and 14). For example, spectral class 8 has the highest reflectance in the Dewey County core, is rich in Ca content (>37%), and possesses a tightly clustered geochemical distribution (Fig. 14). An examination of the reflectance signature associated with each spectral class reveals that Ca-rich samples are associated with high reflectance, whereas increasing Si and Al content are associated with low reflectance (Figs. 13A and 14). While no mineralogical data exists for the Dewey County core, a strong relationship between high reflectance and calcite abundance in conjunction with low reflectance and quartz and clay abundance can be observed in the Canadian County core (Fig. 13B).

Figure 15 presents the spectral class makeup of each lithofacies in the Canadian and Dewey County cores respectively. Lithofacies are listed on the y-axis in order of increasing average Si and Al, content and decreasing average Ca content. There is a strong relationship between the abundance of spectral classes with lower reflectance signatures (i.e., cooler colors) and lithofacies rich in Si and Al. Conversely, spectral classes with higher reflectance signatures denoted by warmer colors are abundant in Ca rich lithofacies.

5. Discussion

5.1. Lithofacies Interpretations

5.1.1. Canadian County Core

The abundant burrowing, low to moderate energy sedimentary structures, and grain size (mud-very fine sand) described in this core are consistent with previous interpretations of a depositional environment that ranged from lower shoreface to offshore shelf during deposition of the Meramec Formation (Shelley, 2016; Price et al., 2020). Lithofacies with higher Ca and calcite contents are interpreted to reflect higher energy deposits that have had high primary, interparticle porosity subsequently occluded by calcite cementation. Conversely, the presence of Al and clay is generally attributed to lower energy distal ramp deposits. Amalgamated beds in lithofacies 5 that consist of clean, calcareous quartz siltstone and very fine sandstone with little mud are interpreted as amalgamated sheet sands repeatedly deposited by subaqueous sediment gravity flows (Price et al., 2020). Little variation in the grain size of detrital input to the system may explain why these turbidite-dominated packages lack graded bedding. Due to its stratigraphic proximity to lithofacies 5, the graded architecture and planar laminations of lithofacies 1 can be interpreted in two ways: distal deposition of finer grained fractions of turbidites (i.e., an autogenic process), and/or subtle variations in relative sea level that cause

changes in depositional proximity to the shoreline (i.e., an allogenic process). Given the paleogeographic setting within a low relief ramp (< 0.1°) (Miller, 2018), even small changes in eustasy may produce a significant change in water depth, with lithofacies 4 and 2 representing low energy offshore shelf deposits and lithofacies 6 and 7 representing higher energy lower shoreface deposits. Lithofacies 7, where present at the base of the Canadian County core, is a quartz silt-bearing carbonate that likely formed the deeper water equivalent to the approximately Osagean skeletal grainstone of lithofacies 6 in the Dewey County Core.

5.1.2. Dewey County Core

The Dewey County core is situated up depositional and structural dip of the Canadian County core, is slightly coarser grained, and includes a greater proportion of detrital calcite bioclasts, minimal burrowing, and less frequent laminations. These observations are consistent with an interpretation of depositional environments ranging from lower shoreface to offshore shelf during deposition of the Meramec Formation. The top of lithofacies 6 and the base of lithofacies 1 bracket the start and end of a period of sea level rise from a shallow, Osagean carbonate complex to a deeper water Chester shale (Price et al., 2020). Lithofacies 5 and 4 are interpreted as an extended deepening transition as carbonate factory conditions in the Osagean are steadily reduced by increasing detrital siliciclastic input during early to middle Meramecian time. Lithofacies 2 overlies lithofacies 5, and is comprised primarily of Si-rich, heavily bioturbated, interbedded medium silt and mud, implying an offshore shelf environment. Inclined beds in lithofacies 3, and the presence of calcite cement indicate reworked sediment, suggested by Price et al. (2020) to be the product of longshore currents.

5.2. Hyperspectral Cyclicity in the Meramec Formation

Previous researchers working on the Meramec Formation in the Anadarko Basin, and regional outcrop equivalents, have largely interpreted these deposits as reflecting several orders of stratigraphic cyclicity associated with changes to eustatic sea level (Coffey, 2000; Shelley, 2016; Godwin, 2017; Miller, 2018; Price et al., 2020). In the STACK Play, Price et al. (2020) described three orders of cyclicity observed in core and well logs, which are designated low, intermediate and high. Due to the lack of biostratigraphic constraints, the durations of these cycles in absolute time are uncertain. Low order cyclicity was interpreted to represent eustatic sea level rise during deposition of the Meramecian following a sharp regional sea level fall toward the conclusion of the Osagean, and capped by a transgressive surface of erosion at the start of the Chesterian (Curtis and Champlin, 1959). Intermediate order cyclicity was interpreted to reflect the superposition of sea level rise-fall-rise on the lower order trend of overall sea level rise during the Meramecian (Price et al., 2020). The stratigraphic record of this intermediate order of cyclicity is manifested as packages of multiple clinoforms that are interpreted as systems tracks (Price et al., 2020). High order cyclicity was attributed to high frequency sea level change, which manifests itself in the stratigraphic record as a series of stacked aggradational and progradational clinoforms that exhibit coarsening upward profiles capped by marine flooding surfaces (Price et al., 2020). These clinoform parasequences comprise the building blocks of systems tracks that govern the intermediate cyclicity described above.

In the biostratigraphically constrained Meramecian outcrops of the Pryor Creek Formation in northeast Oklahoma, Godwin (2017) identified the Meramecian interval as a partial 2^{nd} order cycle of marine transgression and associated sea level rise. Superimposed on 2^{nd} order cycles Godwin (2017) discussed one full and one partial 3^{rd} order cycle which records a period of

sea level rise-fall-rise. Higher frequency, shallowing upwards cycles are also observed and interpreted to be 4th order cycles that are estimated to have a duration between 300 and 550 kyr (Godwin, 2017).

Because absolute age constraints are not available in the subsurface STACK Play, the time duration of cycles defined from HI data in this study are not certain. Herein, these cycles are assigned 1st, 2nd, 3rd, 4th and 5th order, with 1st order cyclicity representing the longest duration. Note that usage of this nomenclature is informal and not intended to correspond to the more formal definitions of these terms sometimes used by sequence stratigraphers (*i.e.* Vail et al., 1977).

Partial and complete 1st and 2nd order cyclicity can be readily identified using various data, including XRD, pXRF, gamma ray, and HI in both the Canadian and Dewey County cores (Figs. 16 and 17). Partial 1st order cycles are preserved in the Dewey and Canadian County cores respectively, which denote a period of overall sea level rise and deepening during deposition of the Meramec Formation, and are recorded in the HI data by an overall vertical increase in low reflectance spectral classes associated with detrital quartz and clay content, and a general fining upwards trend in grain size (Figs. 16 and 17). Because only the lower ~60% of the Meramec Formation was described in the Canadian County core in this study, only a portion of the partial 1st order cycle of sea level rise was identified (Fig. 16). Conversely, the full Meramec Formation was described in the up-dip Dewey County core, where an overall trend of upwards fining is noticeable, and interpreted herein to reflect relative sea level rise, or transgression, that is a portion of a 1st order cycle (Fig. 17). The partial 1st order cycle defined using HI and various data types in this study is interpreted to relate to “low order cyclicity” defined in the STACK Play

well logs in Price et al. (2020) and to "2nd order" cyclicity defined in northeast Oklahoma outcrops (Godwin 2017).

One full 2nd order cycle is preserved in both cores and an additional partial 2nd order cycle can be seen only near the top of the Meramec Formation in the Dewey County core. 2nd order cycles in both cores document sea level rise and fall, where clay and quartz content increase vertically until a package rich in calcite is deposited indicating sea level fall followed by another steady sea level rise (Figs. 16 and 17). The "intermediate order" cyclicity defined by Price et al. (2020) to be indicative of system tracks, and 3rd order cyclicity defined by Godwin (2017) to be at least several million years in length, are interpreted to be equivalent to 2nd order cyclicity in this study.

Four full and one partial 3rd order cycles can be seen in the pXRF, gamma log, and HI data in the down-dip Canadian County core, however, these cycles are below the resolution of XRD data (Fig. 16). Within each of the four complete 3rd order cycles, suites of two lithofacies types typically account for >80% of the cycle. The basal lithofacies type is characteristically rich in quartz and clay, and the overlying lithofacies type is typically more calcareous. 3rd order cycles can generally be described as coarsening upwards sequences of increasing calcite content capped by flooding surfaces rich in clays and quartz. Lithofacies descriptions and HI data identify a general trend of finer-grained, lower energy clay and quartz-rich lithofacies composing the basal half of each 3rd order cycle followed by lithofacies associated with increased depositional energy and calcite content comprising the upper half (Fig. 16). This is corroborated by the vertically increasing abundance of spectral classes associated with higher calcite fractions within each cycle (Fig. 16). 3rd order cycles are interpreted to be equivalent to "high order" cyclicity defined by Price et al. (2020) associated with clinoform growth influenced by higher

frequency sea level fluctuations. The up-dip depositional position and reduced thickness of the Meramec Formation precludes the possibility of accurately mapping any clinoforms, in the Dewey County core and substantiates the notable absence of 3rd order cyclicity within the HI data.

Like 3rd order cycles, 4th order cycles are a product of lithofacies stacking patterns within a parasequence, but at a finer scale and are only observed in conjunction with lithofacies 4 and 1 of the Canadian County core (Fig. 18). 4th order cycles are not observed in the Dewey County core. Fig. 18 presents an expanded section that is primarily composed of lithofacies 4 with lesser abundances of lithofacies 1, revealing three full 4th order cycles of approximately 6 m each and another half cycle. At this scale, the resolution of XRD data with an average sample spacing of 3 m is insufficient to identify 4th order cyclicity (Fig. 18). The gamma ray log displays several upwards-cleaning trends at low resolution that are weakly observable for the upper two and a half 4th order cycles. The basal cycle is only observable using pXRF and HI data (Fig. 18). These cycles are superimposed on the larger coarsening upward profile of each prograding parasequence, and could possibly be a record of high frequency sea level oscillation superimposed on the prograding geometry of the underlying clinoforms. The high frequency coarsening upwards motifs of 4th order cycles in lithofacies 4 and 1 of the Canadian County core suggest similarity to shallowing upwards cycles that Godwin (2020) interpreted in outcrop to be 4th order cycles of high frequency sea level oscillation of between 300 and 550 kyr duration.

5th order cyclicity exists in both cores and is thought to be generated by both eustatic processes and autogenic behavior driven by turbidity currents. 5th order cycles can be seen in lithofacies 1, and 4 of the Canadian County core, and lithofacies 4 of the Dewey County core. 5th order cycles are defined as bed scale fining upwards sequences of no more than 1 m. These

cycles exist well below the effective resolution of all data types except HI, which clearly exposes the fining upward trajectory observed in Fig. 19. Consequently, HI data can identify cm- to dm-scale cyclicity, as well as compositional variation well below the resolution of conventional logging and sampling techniques. The ability for HI to provide bed-scale information suggests this technique may be valuable for characterizing depositional systems and ultimately hydrocarbon reservoirs.

6. Conclusions

The Meramec Formation of the central Oklahoma STACK Play is comprised of proximal and distal ramp deposits that include argillaceous quartz siltstones, calcareous quartz siltstones and sandstones, and lesser grainstones. Sedimentologic descriptions from two drill cores from Canadian and Dewey Counties are used in conjunction with mineralogic and geochemical data to define seven and six lithofacies in each core, respectively. Partial-SWIR (900-1700 nm) hyperspectral imaging data collected from two drill cores were classified and analyzed in conjunction with geochemical and mineralogical data to model a relationship between average spectral reflectance and the abundance of compositional endmembers of quartz, clay, and calcite. Hyperspectral imaging data, together with conventional core data, is shown to distinguish multiple orders of stratigraphic cyclicity in the Meramec Formation, including cyclicity that is below the resolution of typical core logging and sampling procedures. These data suggest that cyclicity in the Meramec Formation likely spans at least five orders, and primarily reflects allocyclic processes driven by both low and high frequency, eustatic sea level fluctuations on a low relief ramp during Late Mississippian time. High-orders of cyclicity may also be attributed to autocyclic processes associated with marine sedimentologic processes, such as deposits generated by storms and episodic turbidity currents.

References

Adão, T., Hruška, J., Pádua, L., Bessa, J., Peres, E., Morais, R., and Sousa, J.J., 2017, Hyperspectral imaging: A review on UAV-based sensors, data processing and applications for agriculture and forestry: Remote Sensing, v. 9, doi:10.3390/rs9111110.

Bachri, I., Hakdaoui, M., Raji, M., Teodoro, A.C., and Benbouziane, A., 2019, Machine learning algorithms for automatic lithological mapping using remote sensing data: A case study from Souk Arbaa Sahel, Sidi Ifni Inlier, Western Anti-Atlas, Morocco: ISPRS International Journal of Geo-Information, v. 8, p. 1–20, doi:10.3390/ijgi8060248.

Ball, M.M., Henry, M.E., and Frezon, S.E., 1991, Petroleum geology of Anadarko Basin Region, Province (115), Kansas, Oklahoma and Texas.:

Burchette, T.P., and Wright, V.P., 1992, Carbonate ramp depositional systems: Sedimentary Geology, v. 79, p. 3–57, doi:10.1016/0037-0738(92)90003-A.

Cecilia Contreras Acosta, I., Khodadadzadeh, M., Tusa, L., Ghamisi, P., and Gloaguen, R., 2019, A Machine Learning Framework for Drill-Core Mineral Mapping Using Hyperspectral and High-Resolution Mineralogical Data Fusion:, doi:10.1109/jstars.2019.2924292.

Chawchai, S., Kylander, M.E., Chabangborn, A., Löwemark, L., and Wohlfarth, B., 2016, Testing commonly used X-ray fluorescence core scanning-based proxies for organic-rich lake sediments and peat: Boreas, v. 45, p. 180–189, doi:10.1111/bor.12145.

Coakley, J.A., 2003, Reflectance and Albedo, Surface: Encyclopedia of Atmospheric Sciences, p. 1914–1923, doi:10.1016/b0-12-227090-8/00069-5.

Coffey, W., 2001, Lithostratigraphy and Porosity Characterization of the Sycamore Formation (Mississippian), and it's Relationship to Reservoir Performance, Carter-Knox Field, Grady and Stephens county, Oklahoma: , p. 9–17, http://archives.datapages.com/data/ocgs/data/052/052001/0009.htm.

Coffey, W.S., 2000, The Diagenetic History and Depositional System of the Sycamore Formation (Mississippian), Carter-Knox Field, Grady and Stephens Counties, Oklahoma, doi:10.16953/deusbed.74839.

Cooper, C.D., and Mustard, J.F., 1999, Effects of Very Fine Particle Size on Reflectance Spectra of Smectite and Palagonitic Soil: Icarus, v. 142, p. 557–570, doi:10.1006/icar.1999.6221.

Curtis, D., and Champlin, S., 1959, Depositional environments of Mississippian limestones of Oklahoma: Tulsa Geological Society Digest, v. 27, p. 90–103, http://archives.datapages.com/data/tgs/digest/data/027/027001/90_tgs270090.htm.

Gewali, U.B., Monteiro, S.T., and Saber, E., 2018, Machine learning based hyperspectral image analysis: A survey: ArXiv, http://arxiv.org/abs/1802.08701.

Godwin, C.J., 2017, Lithostratigraphy and Conodont Biostratigraphy of the Upper Boone group and Mayes Group in the Southwestern Ozarks of Oklahoma, Missouri, Kansas, and Arkansas.

Granath, J.W., 1989, Structural Evolution of the Ardmore Basin, Oklahoma: Tectonics, v. 8, p. 1015–1036.

Greene, J., Kosanke, T.H., and Linton, P., 2019, Quantitative Calibration of Hyperspectral Core Imaging Data : A New Method for Producing Continuous , High-Resolution Mineralogical Characterization of Cores from Both Conventional and Unconventional Reservoirs *:, doi:10.1306/42444Greene2019.

Gutschick, R.C., and Sandberg, C.A., 1983, Mississippian continental margins of the conterminous United States.: Society for Sedimentary Geology, p. 79–96.

Hardwick, J., 2018, Reservoir Quality Evaluation Of The Meramec And Upper Osage Units In The Anadarko Basin, doi:10.1093/imamci/dnt037.

Jacq, K., Giguet-Covex, C., Sabatier, P., Perrette, Y., Fanget, B., Coquin, D., Debret, M., and Arnaud, F., 2019, (Paper) High-resolution grain size distribution of sediment core with hyperspectral imaging: Sedimentary Geology, v. 393–394, p. 105536, doi:10.1016/j.sedgeo.2019.105536.

Jakob, S., Zimmermann, R., and Gloaguen, R., 2017, The Need for Accurate Geometric and Radiometric Corrections of Drone-Borne Hyperspectral Data for Mineral Exploration: MEPHySTo-A Toolbox for Pre-Processing Drone-Borne Hyperspectral Data: Remote Sensing, v. 9, doi:10.3390/rs9010088.

Johnson, K.S., 1989, Geologic evolution of the Anadarko Basin: Oklahoma Geological Survey Circular, v. 90, p. 3–12.

Kirsch, M., Lorenz, S., Zimmermann, R., Tusa, L., Möckel, R., Hödl, P., Booysen, R., Khodadadzadeh, M., and Gloaguen, R., 2018, Integration of terrestrial and drone-borne hyperspectral and photogrammetric sensing methods for exploration mapping and mining monitoring: Remote Sensing, v. 10, doi:10.3390/rs10091366.

Kurz, T.H., Dewit, J., Buckley, S.J., Thurmond, J.B., Hunt, D.W., and Swennen, R., 2012, Hyperspectral image analysis of different carbonate lithologies (limestone, karst and hydrothermal dolomites): The Pozalagua Quarry case study (Cantabria, North-west Spain): Sedimentology, v. 59, p. 623–645, doi:10.1111/j.1365-3091.2011.01269.x.

de Linaje, V.A., Khan, S.D., and Bhattacharya, J., 2018, Study of carbonate concretions using imaging spectroscopy in the Frontier Formation, Wyoming: International Journal of Applied Earth Observation and Geoinformation, v. 66, p. 82–92, doi:10.1016/j.jag.2017.11.010.

Lorenz, S., Seidel, P., Ghamisi, P., Zimmermann, R., Tusa, L., Khodadadzadeh, M., Contreras, I.C., and Gloaguen, R., 2019, Multi-Sensor Spectral Imaging of Geological Samples: A Data Fusion Approach Using Spatio-Spectral Feature Extraction: Sensors (Basel, Switzerland), v. 19, doi:10.3390/s19122787.

van der Meer, F., 2004, Analysis of spectral absorption features in hyperspectral imagery: International Journal of Applied Earth Observation and Geoinformation, v. 5, p. 55–68, doi:10.1016/j.jag.2003.09.001.

Miller, J., 2018, Regional Stratigraphy and Organic Richness of the Mississiippian Meramec and Associated Strata, Anadarko Basin, Central Oklahoma, doi:10.1051/matecconf/201712107005.

Mohamed, E.S., Saleh, A.M., Belal, A.B., and Gad, A.A., 2018, Application of near-infrared reflectance for quantitative assessment of soil properties: Egyptian Journal of Remote Sensing and Space Science, v. 21, p. 1–14, doi:10.1016/j.ejrs.2017.02.001.

Nardin, E., Goddéris, Y., Donnadieu, Y., Le Hir, G., Blakey, R.C., Pucéat, E., and Aretz, M., 2011, Modeling the early Paleozoic long-term climatic trend: Bulletin of the Geological Society of America, v. 123, p. 1181–1192, doi:10.1130/B30364.1.

Nieminski, N.M., and Graham, S.A., 2017, Modeling Stratigraphic Architecture Using Small Unmanned Aerial Vehicles and Photogrammetry: Examples From the Miocene East Coast Basin, New Zealand: Journal of Sedimentary Research, v. 87, p. 126–132, doi:10.2110/jsr.2017.5.

Notesco, G., Ogen, Y., and Ben-Dor, E., 2015, Mineral classification of makhtesh ramon in israel using hyperspectral longwave infrared (LWIR) remote-sensing data: Remote Sensing, v. 7, p. 12282–12296, doi:10.3390/rs70912282.

Okyay, Ü., Khan, S.D., Lakshmikantha, M.R., and Sarmiento, S., 2016, Ground-based hyperspectral image analysis of the lower Mississippian (Osagean) reeds spring formation rocks in southwestern Missouri: Remote Sensing, v. 8, doi:10.3390/rs8121018.

Perry, W.J., 1989, Tectonic evolution of the Anadarko Basin Region, Oklahoma: US Geological Survey Bulletin, v. 1866 A.

Price, B.J., Pollack, A.C., Lamb, A.P., Peryam, T.C., and Anderson, J.R., 2020, Depositional interpretation and sequence stratigraphic control on reservoir quality and distribution in the Meramecian STACK play Depositional interpretation and sequence stratigraphic control on reservoir quality and 1 distribution in the Meramecian STAC: AAPG Bulletin, v. 104, p. 357–386, doi:10.1306/04301917411.

Rogers, S.M., 2001, Deposition and diagenesis of mississippian chat reservoirs, North-central Oklahoma: AAPG Bulletin, v. 85, p. 115–129.

van Ruitenbeek, F.J.A., Debba, P., van der Meer, F.D., Cudahy, T., van der Meijde, M., and Hale, M., 2006, Mapping white micas and their absorption wavelengths using hyperspectral band ratios: Remote Sensing of Environment, v. 102, p. 211–222, doi:10.1016/j.rse.2006.02.012.

Satterfield, T., and Standridge, R., 2017, The Age of Oklahom ’s Mountain Ranges: Oklahoma Geology Notes, v. 76.

Shelley, S.A., 2016, Outcrop-Based Sequence Stratigraphy and Reservoir Characterization of an Upper Mississippian Mixed Carbonate- Siliciclastic Ramp, Mayes County, Oklahoma.

Simms, J., and Simms, F., 1995, The Geology of the Southwestern Ozark Uplift.:

Stright, L., Stewart, J., Campion, K., and Graham, S., 2014, Geologic and seismic modeling of a coarse-grained deep-water channel reservoir analog (Black’s Beach, La Jolla, California): AAPG Bulletin, v. 98, p. 695–728, doi:10.1306/09121312211.

Sun, L., Khan, S.D., Sarmiento, S., Lakshmikantha, M.R., and Zhou, H., 2017, Ground-based hyperspectral imaging and terrestrial laser scanning for fracture characterization in the Mississippian Boone Formation: International Journal of Applied Earth Observation and Geoinformation, v. 63, p. 222–233, doi:10.1016/j.jag.2017.08.008.

Sun, L., Khan, S., and Shabestari, P., 2019, Integrated hyperspectral and geochemical study of sediment-hosted disseminated gold at the Goldstrike District, Utah: Remote Sensing, v. 11, doi:10.3390/rs11171987.

Turmelle, T.J., 1982, Lithostratigraphy and Deposistional Environments of the Mayes Formation (Mississippian) in Adair County, Oklahoma.

Vail, P.R., Mitchum Jr., R.M., and Thompson III, S., 1977, Seismic Stratigraphy and Global Changes of Sea Level, Part 4: Global Cycles of Relative Changes of Sea Level.: AAPG Memoir, v. 26, p. 83–98.

Vermeesch, P., 2019, Exploratory Analysis of Provenance Data Using R and the Provenance Package: Minerals, v. 9, p. 193, doi:10.3390/min9030193.

Zaini, N., van der Meer, F., and van der Werff, H., 2014, Determination of carbonate rock chemistry using laboratory-based hyperspectral imagery: Remote Sensing, v. 6, p. 4149–4172, doi:10.3390/rs6054149.

Zaini, N., van der Meer, F., and van der Werff, H., 2012, Effect of grain size and mineral mixing on carbonate absorption features in the SWIR and TIR wavelength regions: Remote Sensing, v. 4, p. 987–1003, doi:10.3390/rs4040987.

Zaini, N., van der Meer, F., and van der Werff, H., 2014, Determination of carbonate rock chemistry using laboratory-based hyperspectral imagery: Remote Sensing, v. 6, p. 4149–4172, doi:10.3390/rs6054149.

Figures

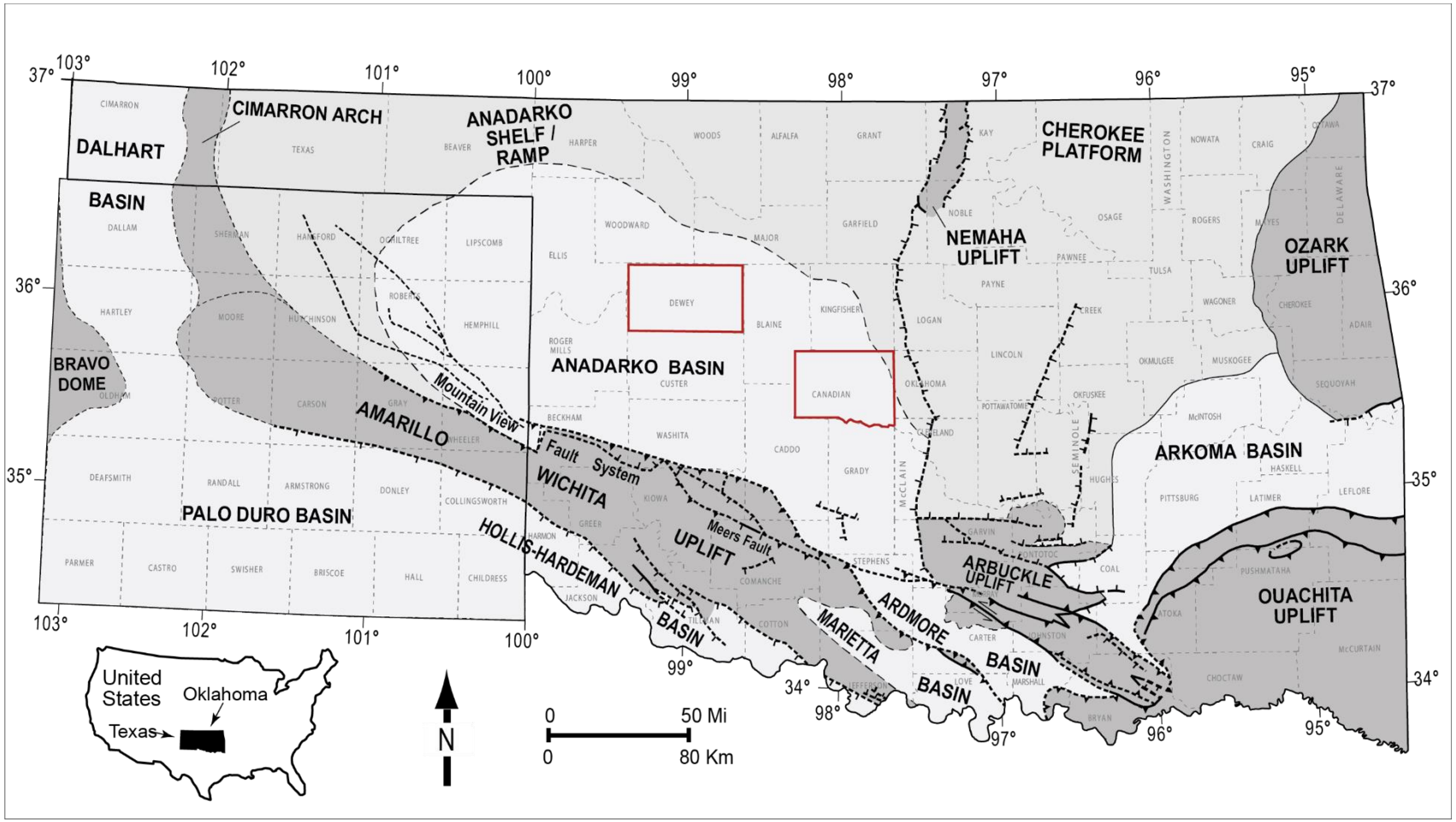

Figure 1. Structural provinces of Oklahoma. Drill cores used in this study are from Dewey and Canadian Counties, outlined in red. Adapted from Miller, 2018.

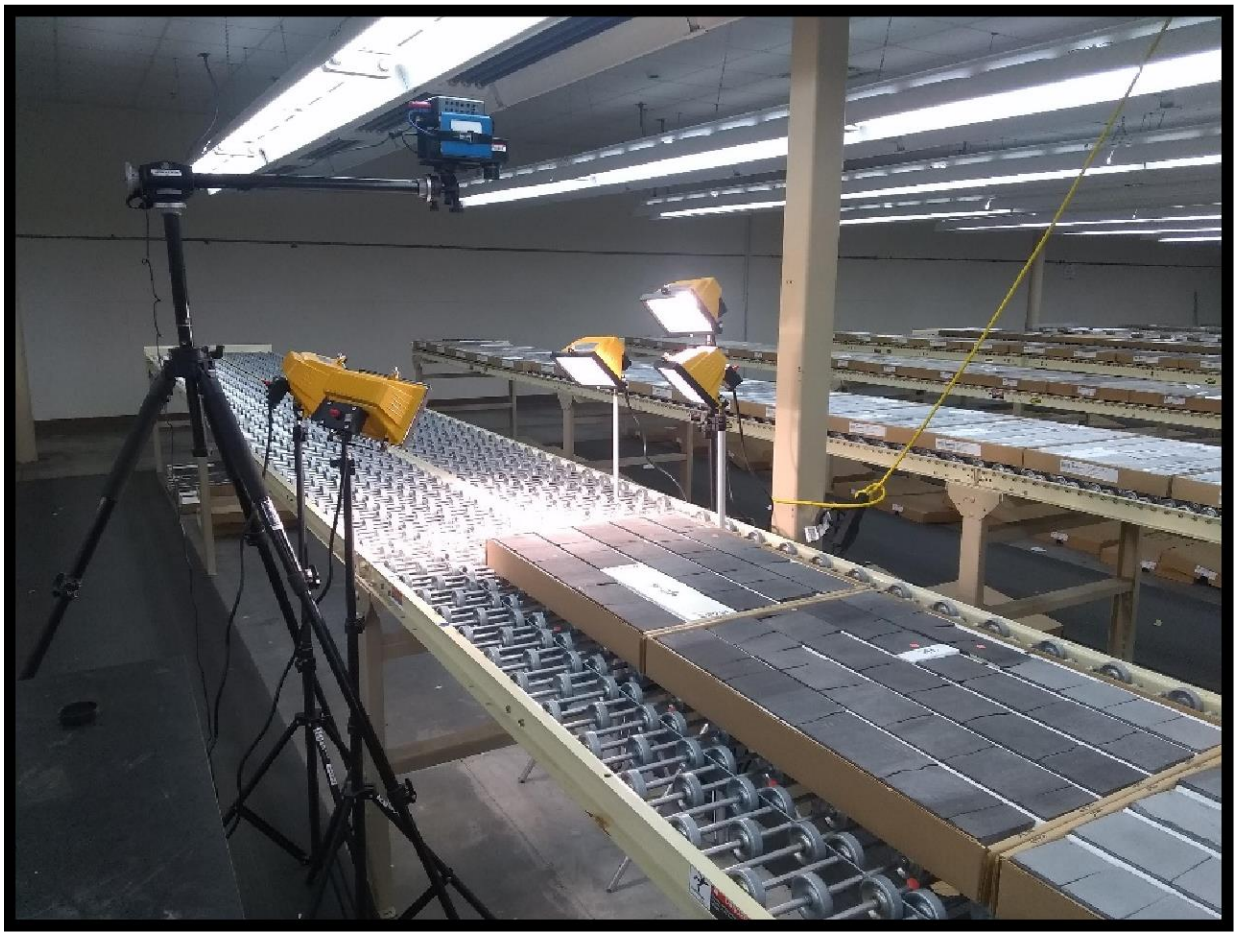

Figure 2. Hyperspectral imaging laboratory setup.

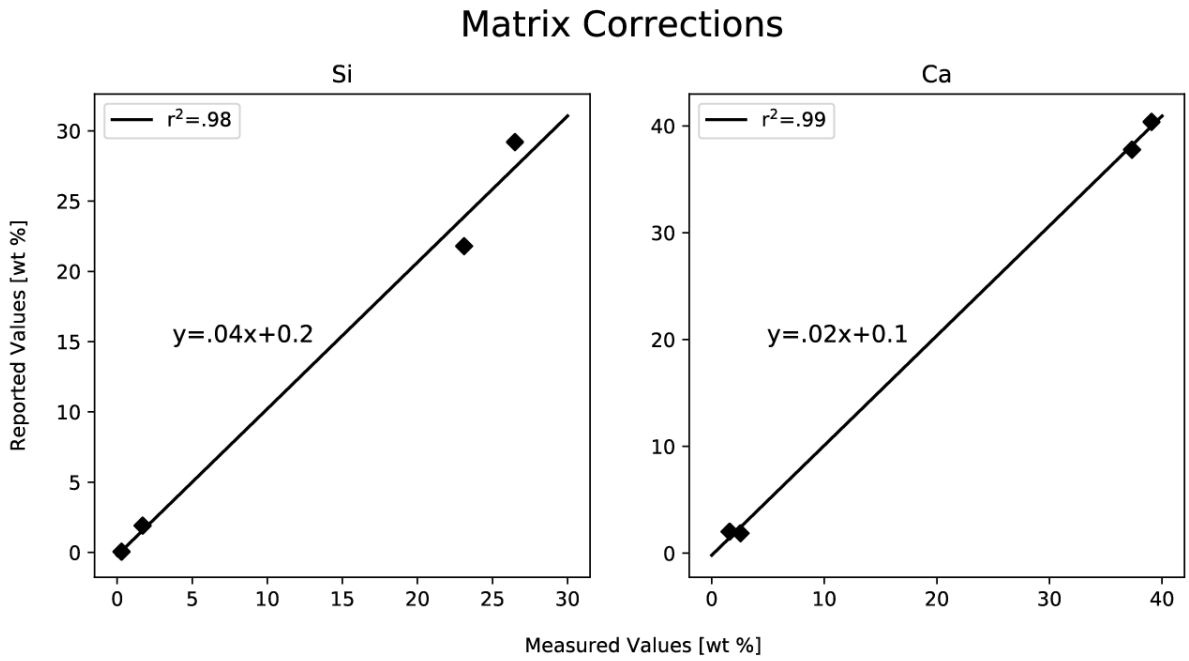

Figure 3. Linear interpolation matrix correction models used to calibrate Si and Ca pXRF data. See text for details.

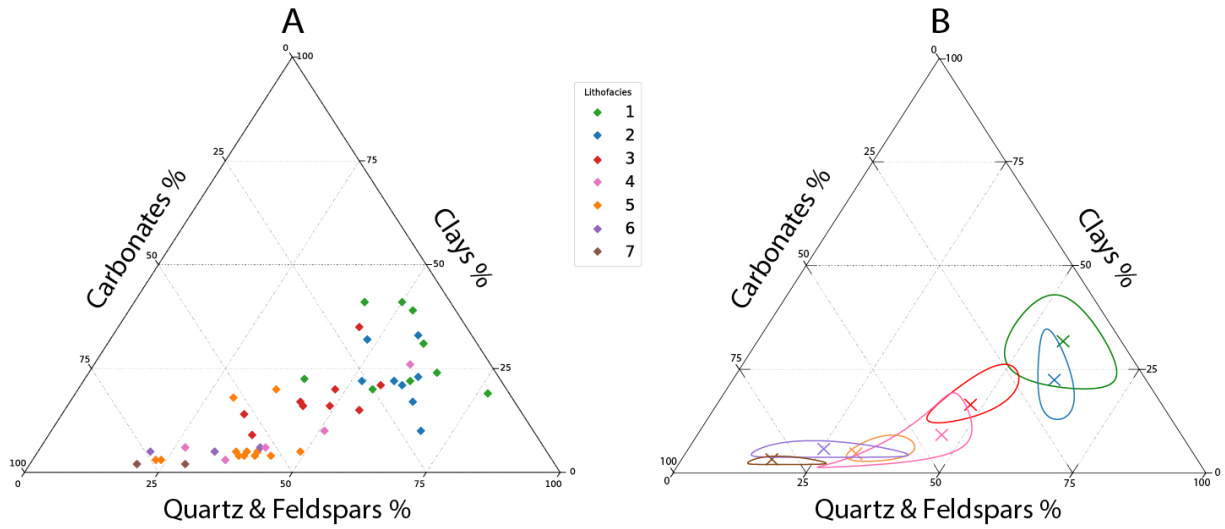

Figure 4. XRD results by lithofacies type in the Canadian County core. (A) XRD data colored by lithofacies type. (B) 95% confidence intervals and mean values for each lithofacies type are denoted by the colored polygons and "X" respectively. Calculated using the provenance R library of (Vermeesch, 2019).

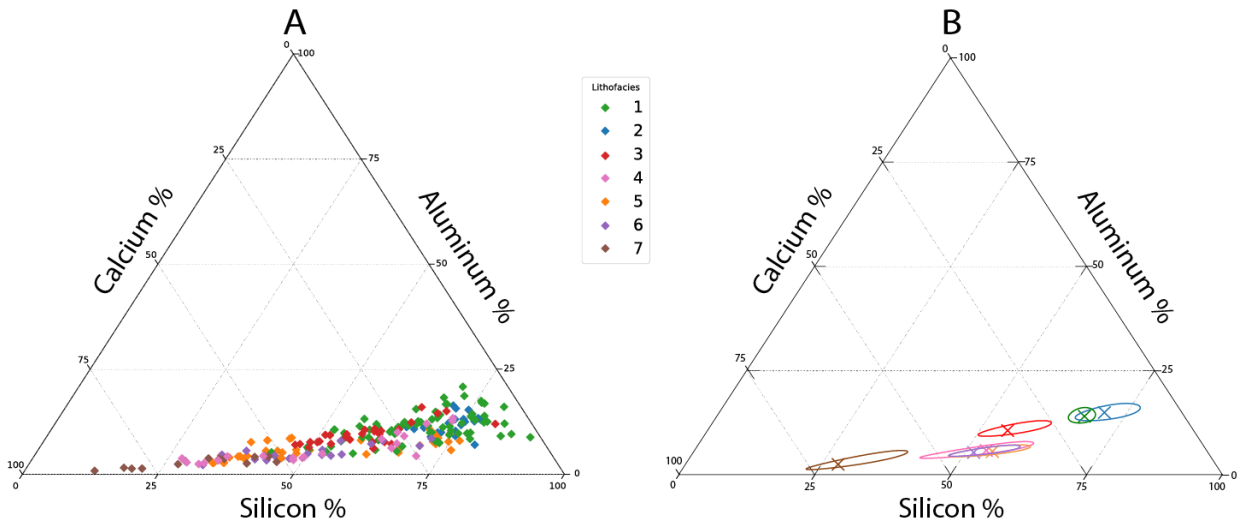

Figure 5. pXRF results by lithofacies type in the Canadian County core. (A) pXRF data colored by lithofacies type. (B) 95% confidence intervals and mean values for each lithofacies type are denoted by the colored polygons and "X" respectively. Calculated using the provenance R library of (Vermeesch, 2019).

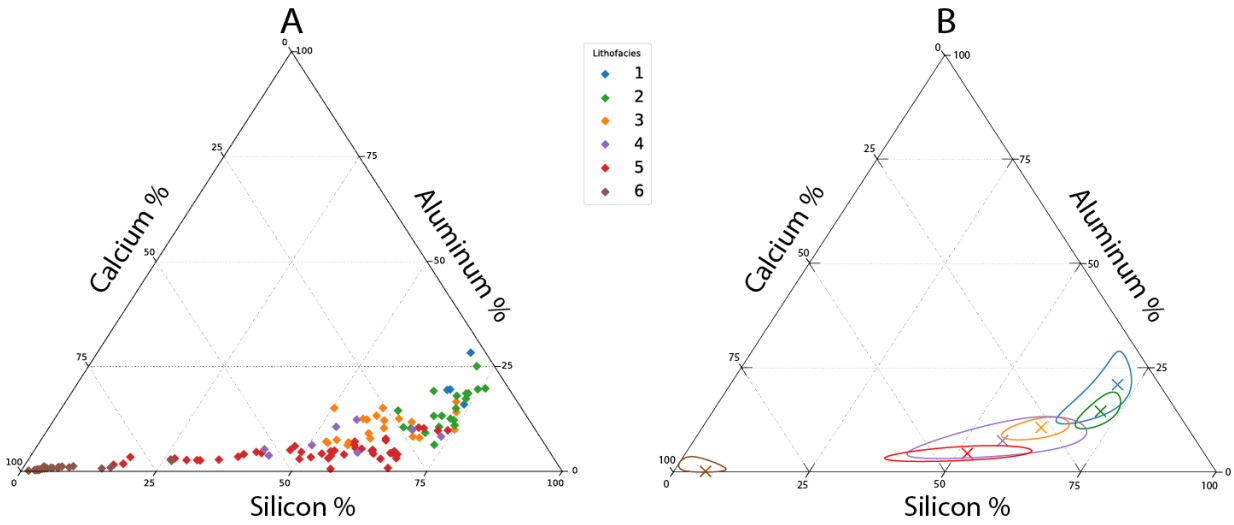

Figure 6. pXRF results by lithofacies type in the Dewey County core. (A) pXRF data colored by lithofacies type. (B) 95% confidence intervals and mean values for each lithofacies type are denoted by the colored polygons and "X" respectively. Calculated using the provenance R library of (Vermeesch, 2019).

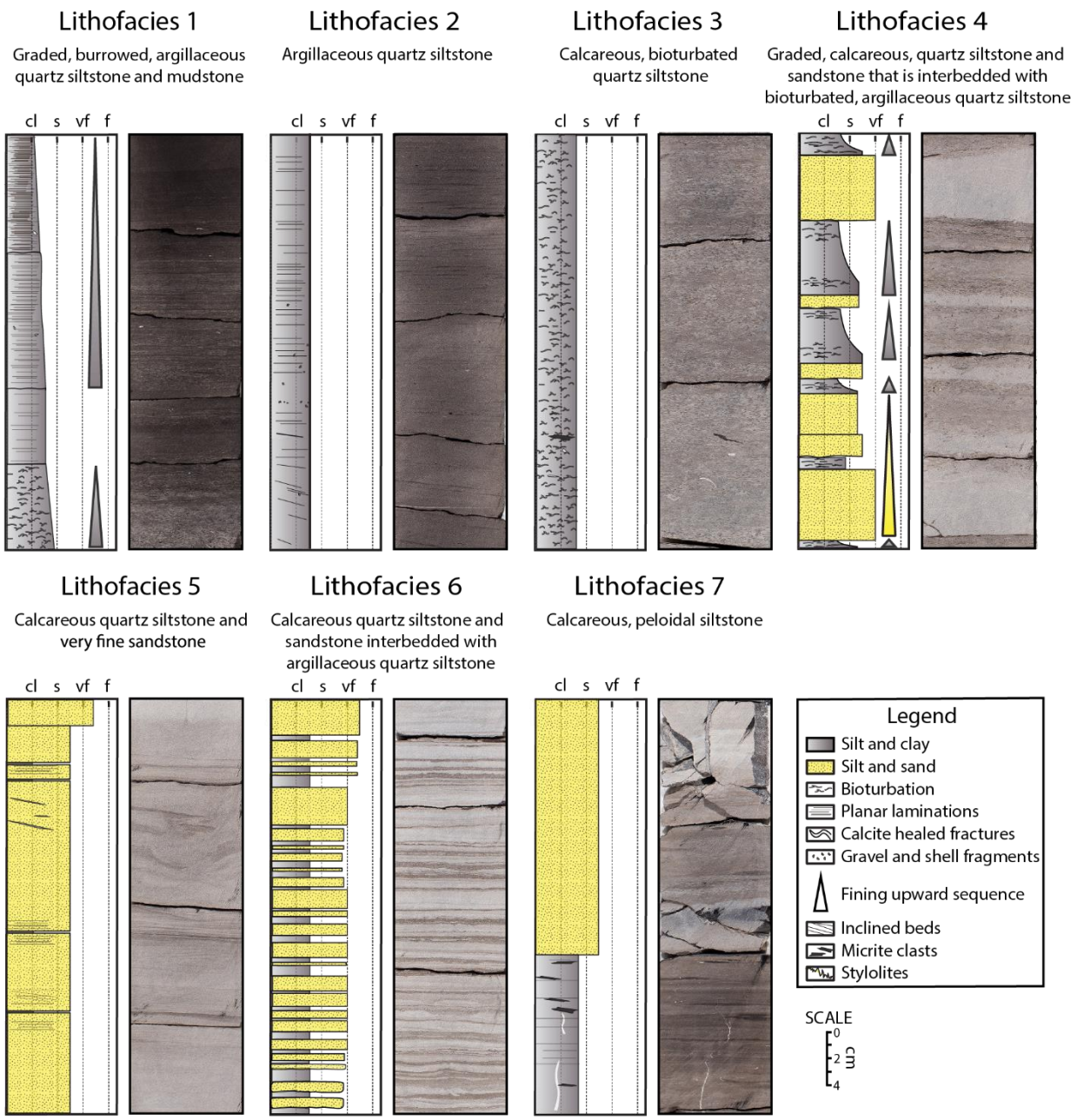

Figure 7. Characteristic 0.30 m (1 ft) measured sections and accompanying core photographs of lithofacies from the Canadian County core. See text for a description of each lithofacies. Abbreviations: cl-clay; s-silt; vf-very fine sand; f-fine sand.

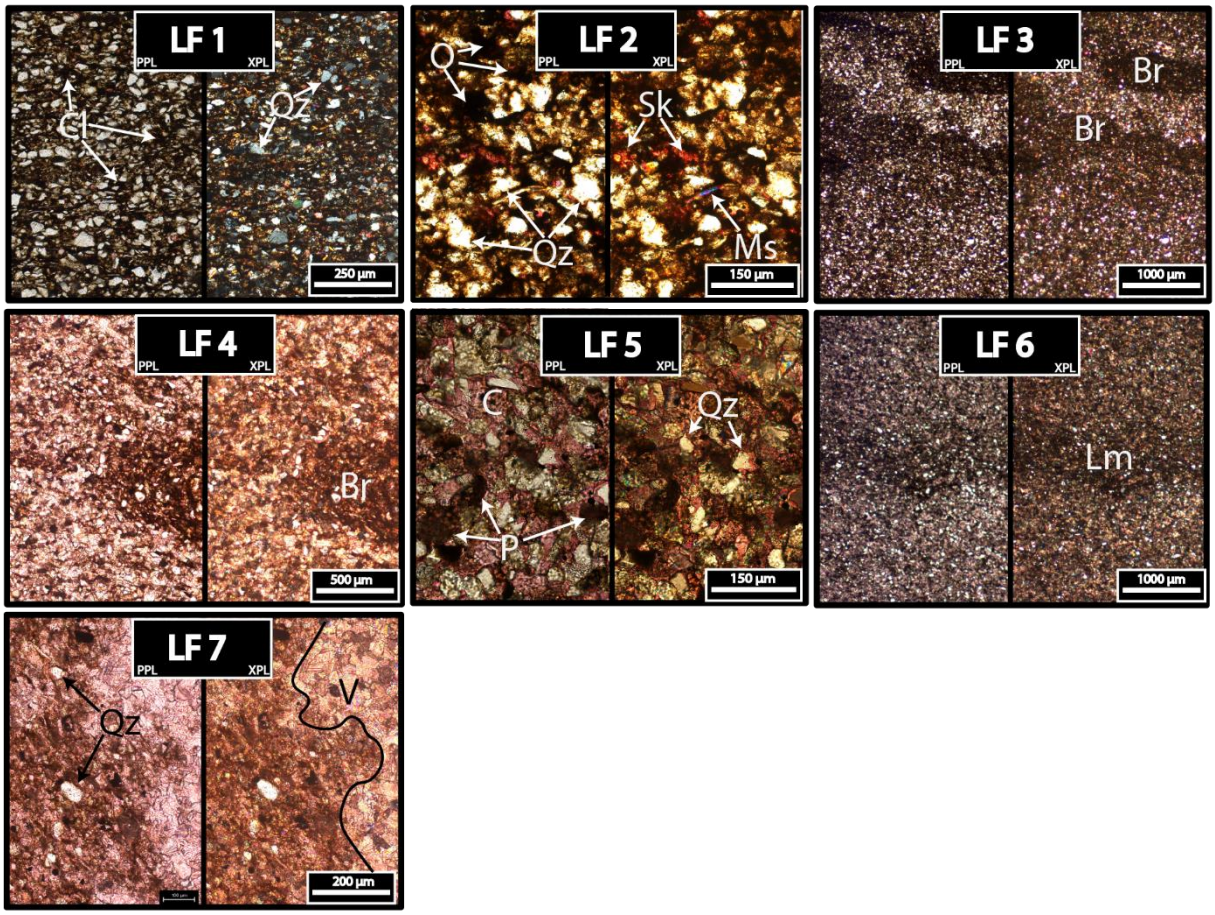

Figure 8. Thin section photomicrographs of each lithofacies from the Canadian County core. Calcite is stained with alizarin Red S. The left side of each image is photographed with plain-polarized light and the right side with crossed-polarized light. Abbreviations: Br-clay filled burrows; C-cement; Cl-clay; LF-lithofacies; Lm-lamination; Ms-muscovite; O-organics; P-peloids; Qz-quartz; Sk-skeletal fragments; V-vein

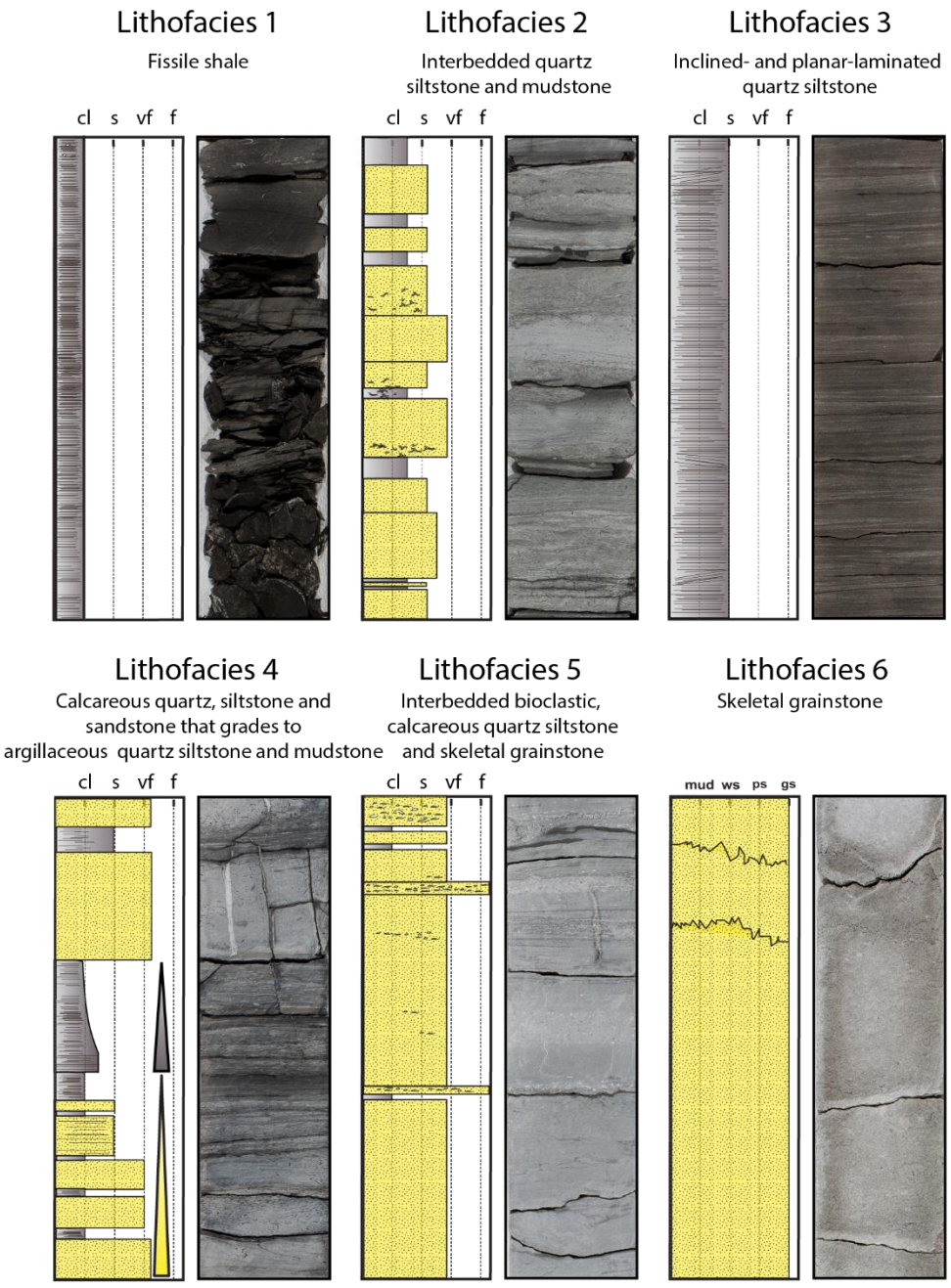

Figure 9. Characteristic 0.30 m (1 ft) measured sections and accompanying core photographs of lithofacies from the Dewey County core. See text for a description of each lithofacies. Abbreviations: cl-clay; f-fine sand; gs-grainstone; ps-packstone; s-silt; vf-very fine sand; ws-wackestone.

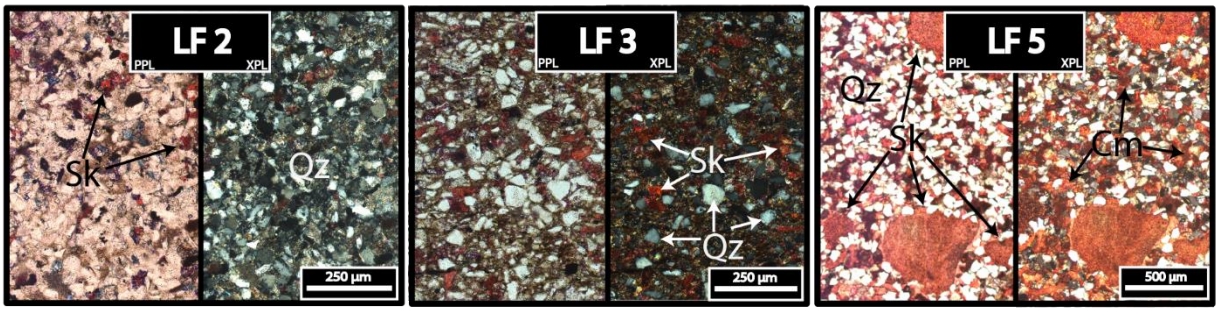

Figure 10. Thin section photomicrographs of selected lithofacies from the Dewey County core. Calcite is stained with alizarin red-s. The left side of each image is photographed with plain-polarized light and the right side with crossed-polarized light. Note: lithofacies 1, 4, and 6 are not pictured. Abbreviations: C-cement; Sk-skeletal fragment; Qz-quartz.

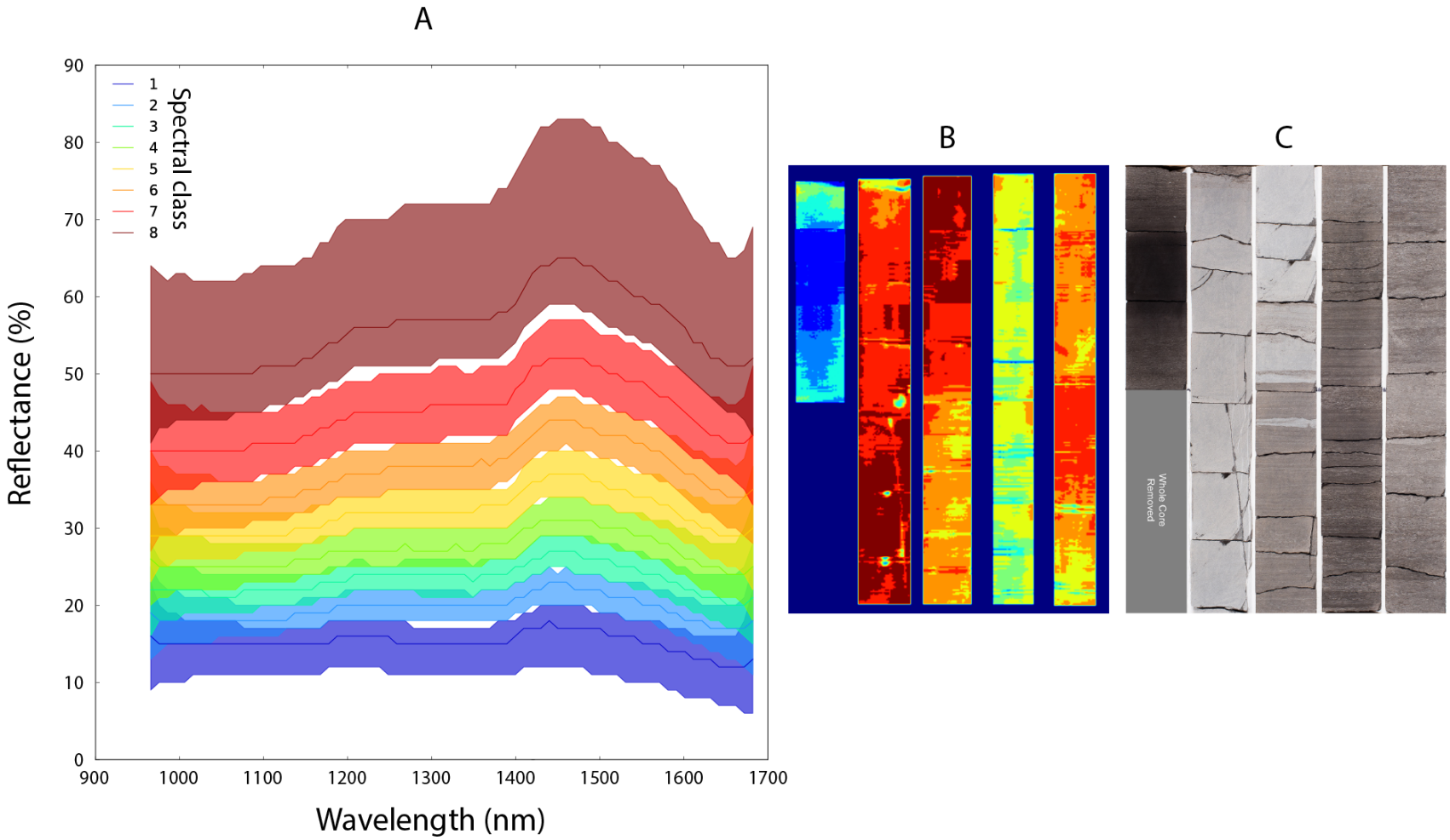

Figure 11. A) Spectral signatures of each spectral class for the Canadian County core. Line indicates median value and colored regions demarcate 10th and 90th percentiles. B) Example of the spatial distribution of spectral classes within a ~3 m (10 ft) interval of core. C) Core photographs of the same core illustrated in (B).

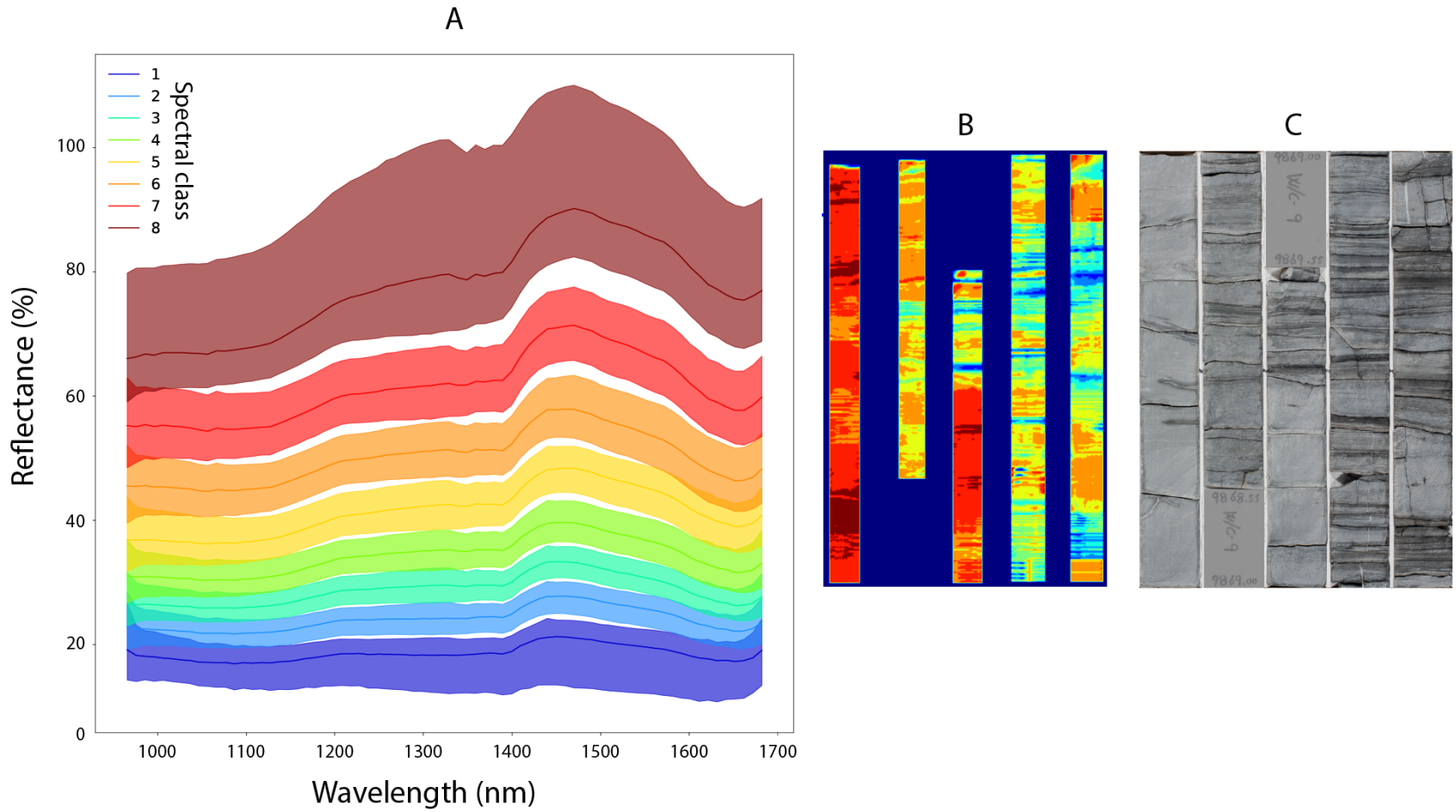

Figure 12. A) Spectral signatures of each spectral class for the Dewey County core. Line indicates median value and colored regions demarcate 10th and 90th percentiles. B) Example of the spatial distribution of spectral classes within a ~3 m (10 ft) interval of core. C) Core photographs of the same core illustrated in (B).

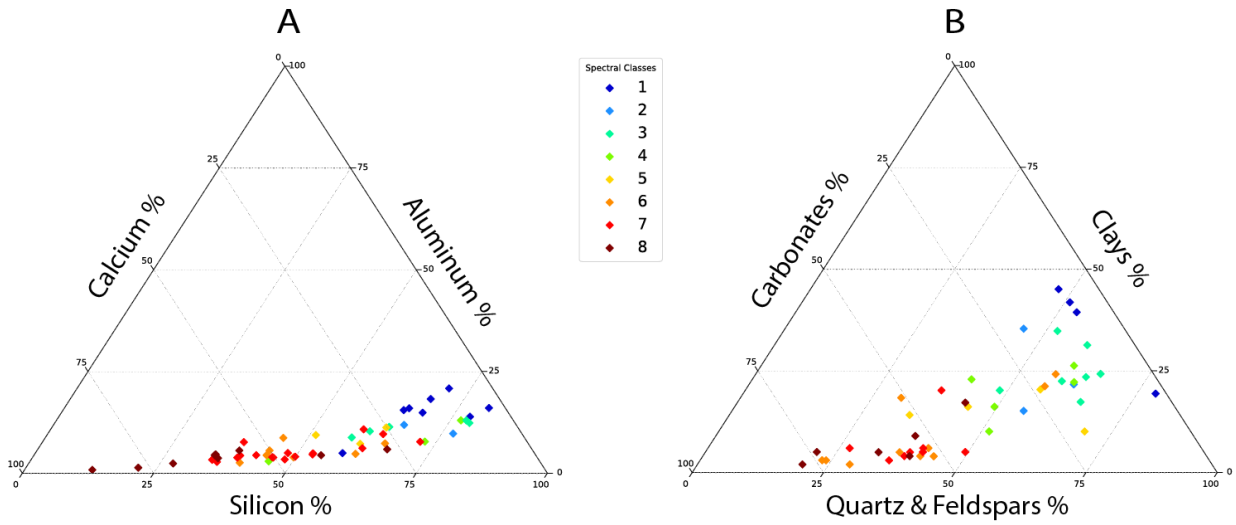

Figure 13. Canadian County core geochemical and mineralogic data colored by dominant spectral class. pXRF and XRD data points were selected where a single hyperspectral class exceeded 90% of the surface area within 1 cm of the data point. A) Geochemistry (pXRF) data. B) Mineralogy (XRD) data.

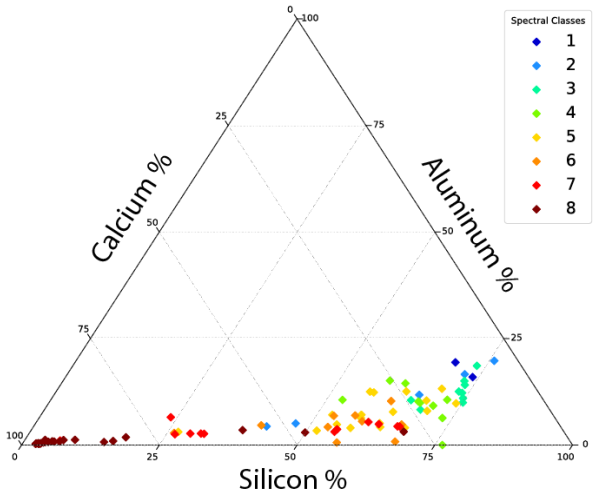

Figure 14. Dewey County core geochemical data (pXRF) colored by dominant spectral class. pXRF data points were selected where a single hyperspectral class exceeded 90% of the surface area within 1 cm of the data point.

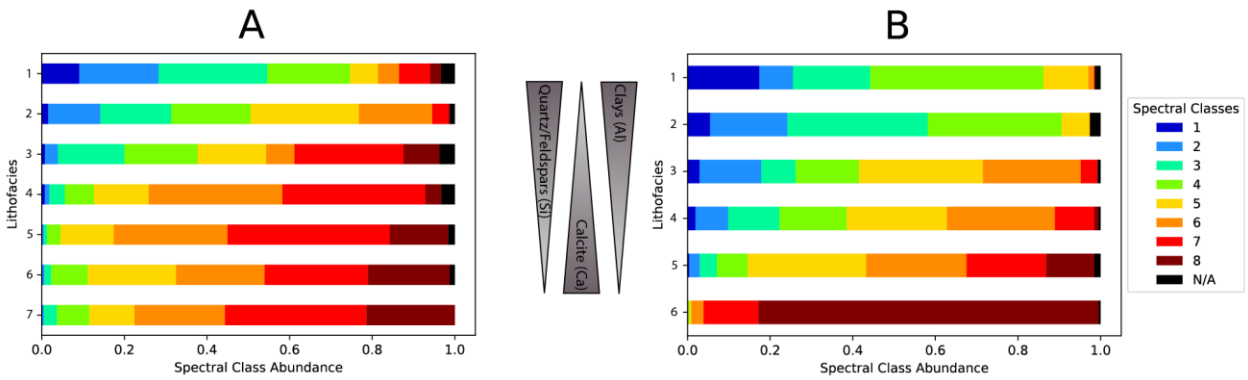

Figure 15. Spectral class abundance of each lithofacies sorted in order of decreasing quartz (Si) and clay (Al) and increasing calcite (Ca) abundance. (A) Canadian County core. (B) Dewey County core.

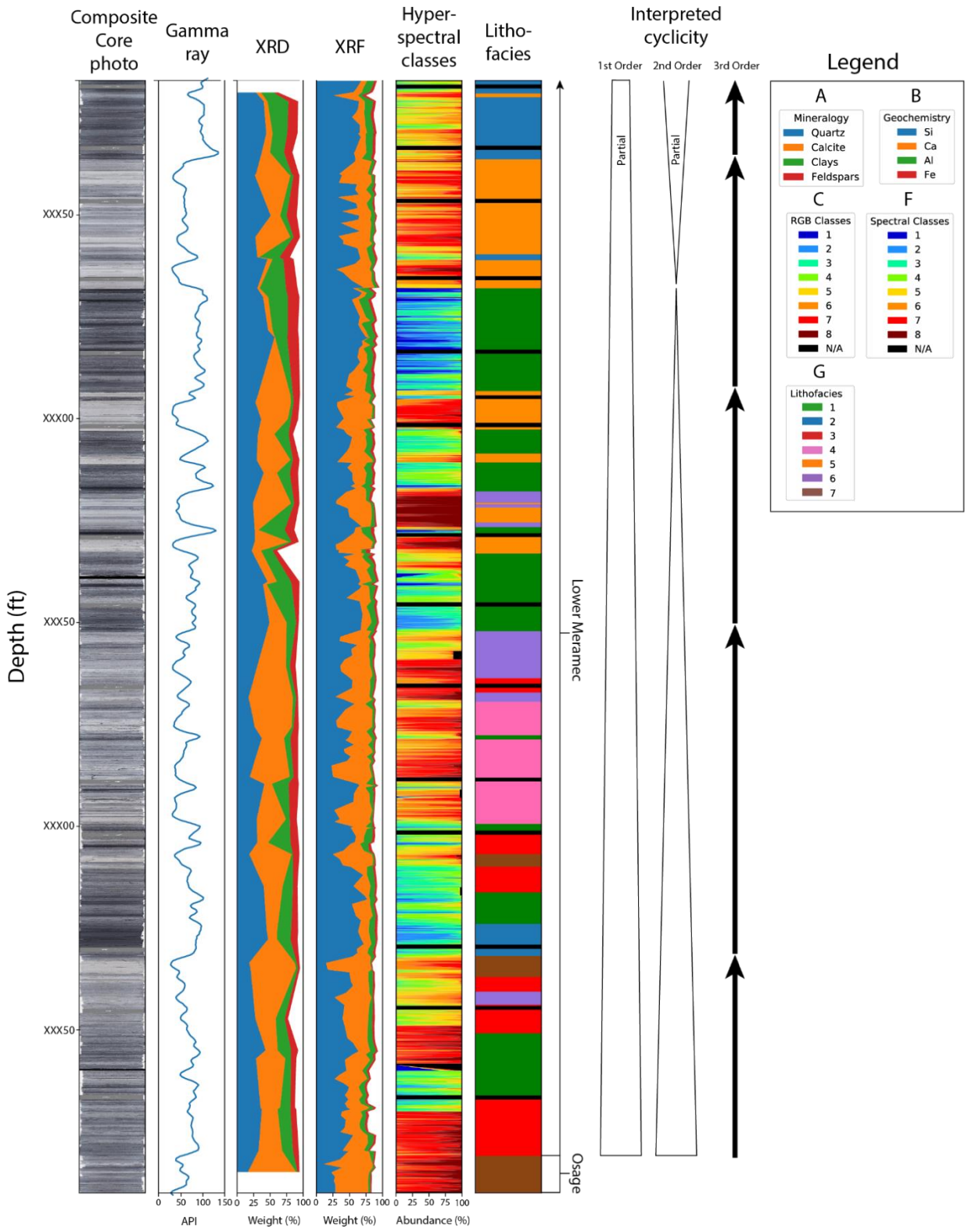

Figure 16. Depth referenced data and interpreted stratigraphic cyclicity for the Canadian County core. Upright triangles indicate sea level rise and inverted triangles indicate sea level fall. Black arrows indicate parasequences.

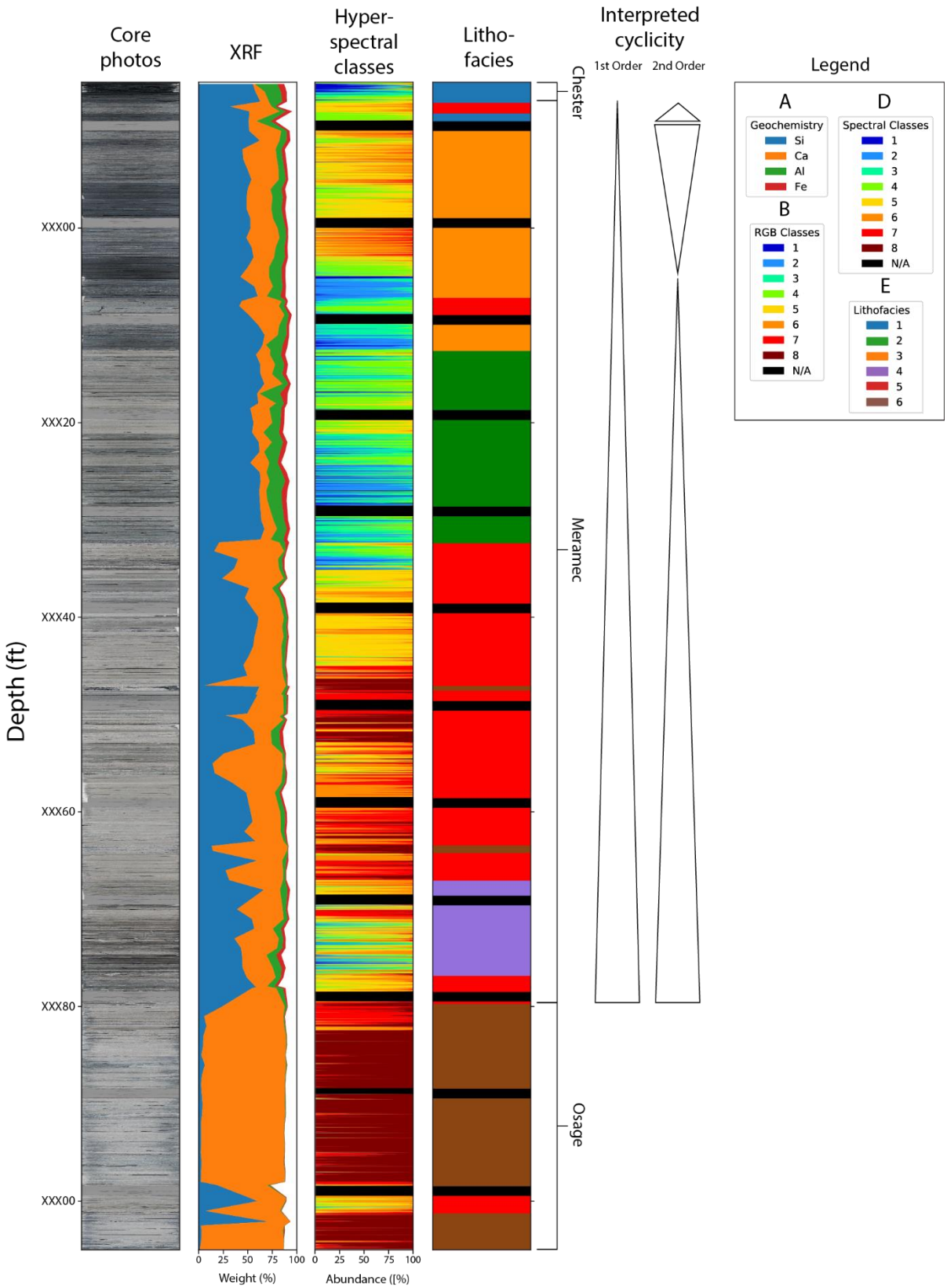

Figure 17. Depth referenced data and interpreted stratigraphic cyclicity for the Dewey County core. Upright triangles indicate sea level rise and inverted triangles indicate sea level fall.

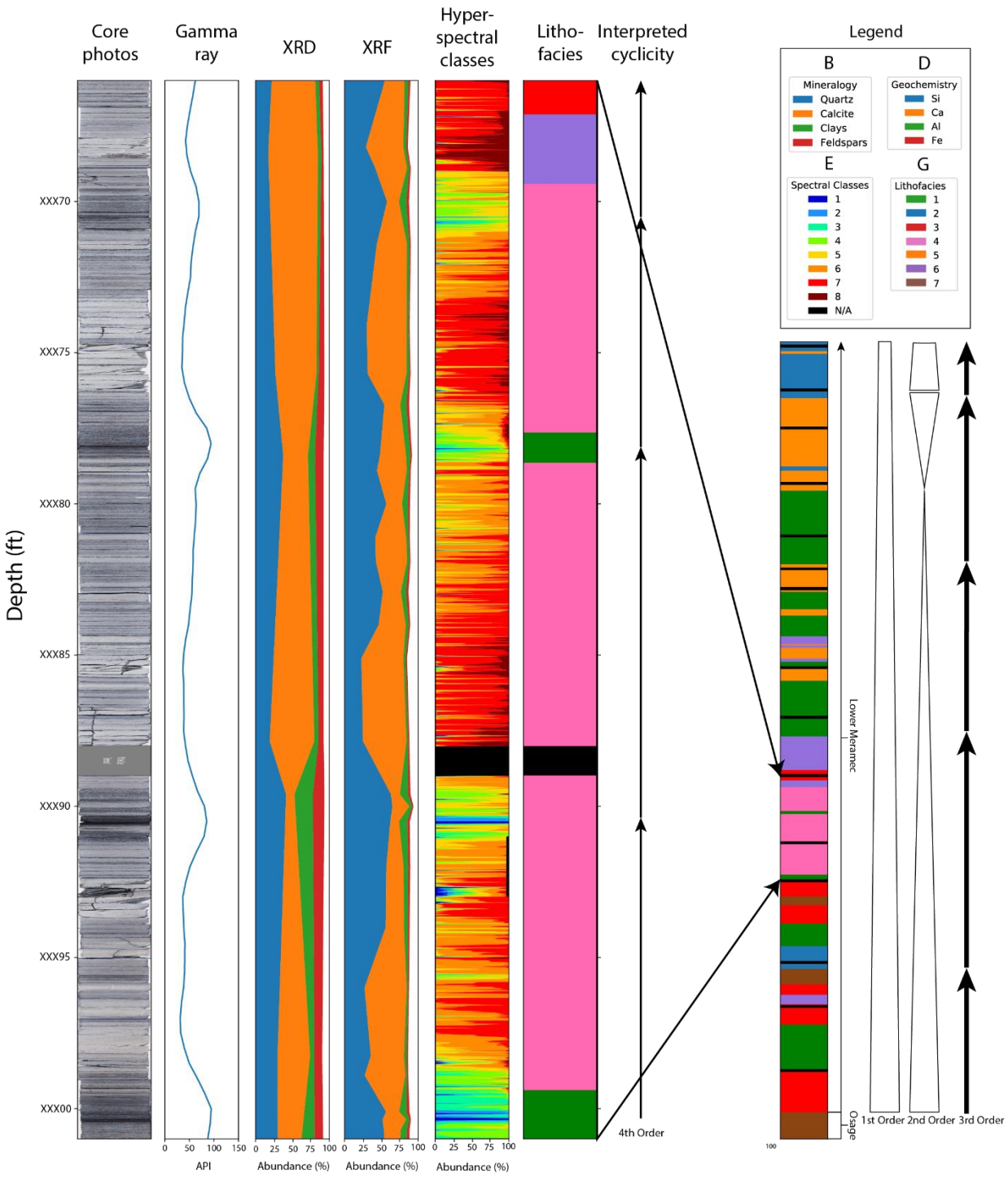

Figure 18. Expanded section of the Canadian County core, outlining 4th order cyclicity. Black arrows indicate 4th order cyclicity.

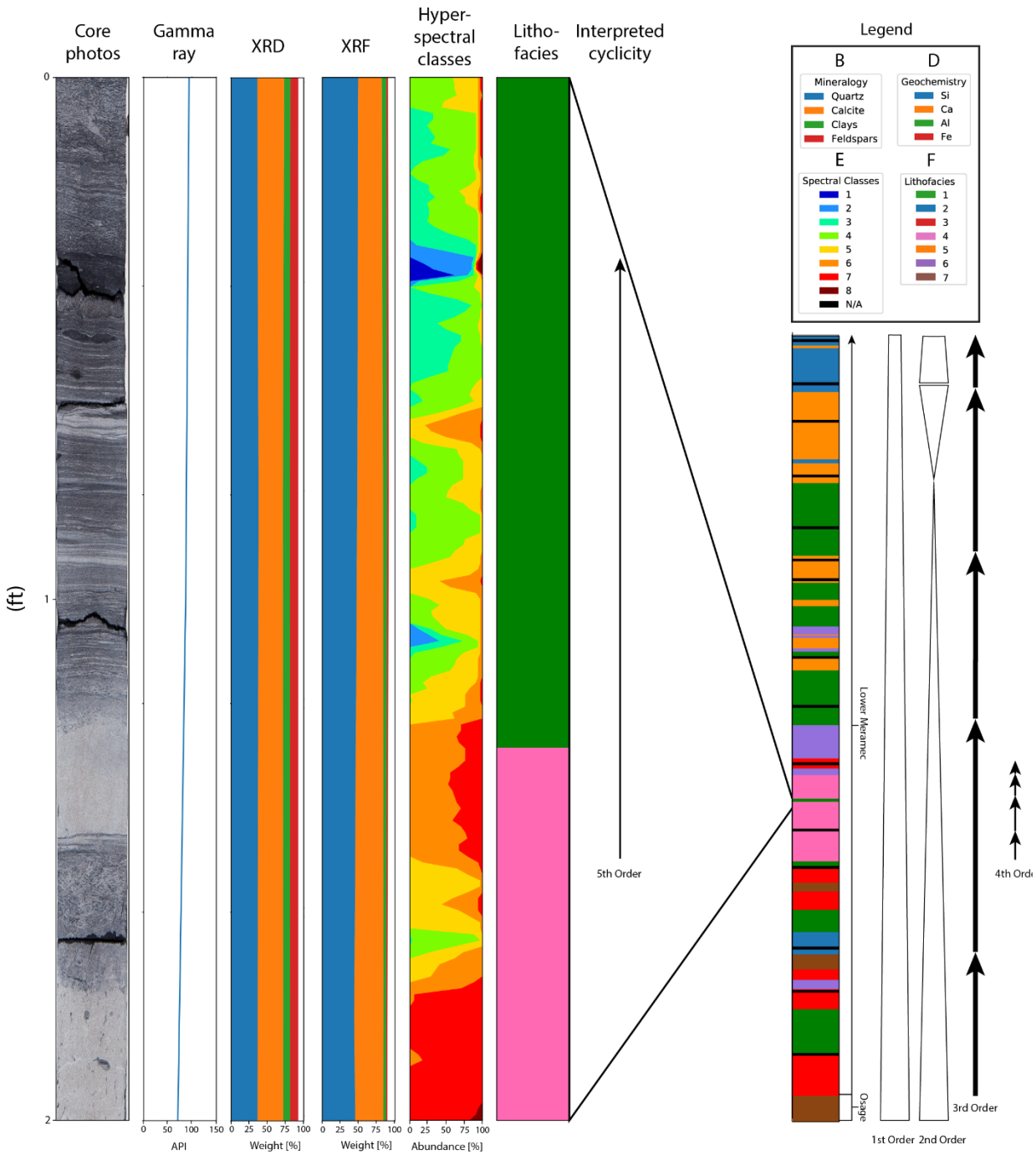

Figure 19. Expanded section of the Canadian County core, outlining 5th order cyclicity. Black arrow indicates a 5th order cycle.

Chapter 3

Sedimentological, Geochemical, and Hyperspectral Characterization of Meramecian-Chesterian Section, Pryor Quarry, Oklahoma

Abstract

The ability to characterize the mineralogic composition of outcrops that are inaccessible from the ground is potentially enhanced using small unmanned aircraft systems (sUAS)-based hyperspectral imaging. In recent years, studies have examined the biostratigraphy, sequence stratigraphy, and lithostratigraphy of Meramecian and Chesterian outcrops of northeastern Oklahoma. However much less work has been dedicated to describing the mineralogy and elemental geochemistry of these outcrops in detail, partly due to the inaccessibility of high outcrop walls. This study characterizes a 21 m (70 ft) outcrop transect in Pryor Quarry, Oklahoma, through descriptions of lithology, collection of pXRF data to provide elemental geochemistry, and measurement of point spectroscopy (350-2500 nm) as a means of ground truthing the results of a sUAS-based partial-SWIR (Short Wave Infrared, 900-1700 nm) hyperspectral imaging survey. Additionally, the effects of outcrop weathering on point spectroscopy data were inspected. Results document the presence of four primary lithofacies in outcrop including grainstone and packstone, wackestone, argillaceous quartz mudstone, and quartz siltstone. Point spectroscopy data suggest that the products of physical and chemical weathering can strongly influence the spectral reflectivity of rock outcrops in the partial-SWIR. Furthermore, a discussion of illumination geometry highlights the serious technical issues associated with normalizing incident intensity values in a field setting for sUAS-based hyperspectral outcrop imaging.

1. Introduction

Interest in outcrop exposures of Meramecian and Chesterian strata in northeast Oklahoma has been spurred by the emergence of the central Oklahoma STACK Play as a producing, unconventional reservoir in the midcontinent (Godwin, 2017). Previous studies at Pryor Quarry in Mayes County, Oklahoma, have sought to characterize these outcrops as analogs to the producing STACK Play by examining their age, depositional setting, and reservoir properties (Shelley, 2016; Godwin, 2017). Meramecian and Chesterian strata within Pryor Quarry are interpreted generally as deposition in a distally-steepened ramp environment, ranging from outer ramp to ramp-crest shoal environments (Turmelle, 1982; Burchette and Wright, 1992; Shelley, 2016; Godwin, 2017). In central Oklahoma, the approximately coeval Meramec Formation of the STACK Play rests on the northeastern shelf of the Anadarko Basin and represents a more distally situated ramp system compared to the Pryor Quarry, and comprises a series of prograding clinoforms, or parasequences, associated with sea level fall (Price et al., 2020). In general, true limestones are rare in the Meramec Formation, which is dominated by finer grained, primarily siliciclastic deposition in deeper water environments ranging from lower shoreface to offshore shelf (Coffey, 2001; Miller, 2018; Price et al., 2020).

In recent years, sUAS have been utilized to photo-document outcrop exposures and construct geometrically corrected photogrammetric models for cm-scale analysis of stratigraphic architecture (Stright et al., 2014; Nieminski and Graham, 2017). While conventional photogrammetric techniques provide invaluable information for outcrop characterization, they do little to determine the mineralogy of the component lithologies in an outcrop. Conversely, hyperspectral sensing techniques have long proven to be a viable means of approximating the

mineralogy of land areas using satellite data, and of rock outcrops using ground based systems (Okyay et al., 2016; Sun et al., 2017, 2019).

The spectral range between 1900 and 2500nm is critical for capturing absorption features necessary for identifying the presence and abundance of common sedimentary minerals including, various clays, and calcite (Cooper and Mustard, 1999; van der Meer, 2004; Mohamed et al., 2018). However, full-SWIR (1000-2500 nm) hyperspectral imaging sensors can cost in excess of 100,000$. Given the financial challenges of acquiring a full-SWIR sUAS, assessing the viability of sUAS-based partial-SWIR (900-1700 nm) hyperspectral imaging sensors for outcrop studies was attempted by mounting a BaySpec partial-SWIR hyperspectral sensor to a DJI Matrice 600 Pro Hexacopter. Unfortunately, equipment failure and software issues rendered the data for this portion of the study unusable. Consequently, chapter 3 focuses on assessing the potential viability of the partial-SWIR (900-1700 nm) HI system for outcrop study by examining point spectroscopy (350-2500nm) and portable X-ray fluorescence (pXRF) data collected on 62 samples from an outcrop with four distinctive lithofacies. For the purposes of determining the viability of sUAS-based hyperspectral imaging for outcrop analysis, only the partial-SWIR (900-1700 nm) range of the 350-2500 nm point spectroscopy data was considered. Because partial-SWIR data lacks distinctive sedimentary mineral absorption features that are predominantly in the 1900-2500 nm range, use of this method to discriminate mineralogy and lithofacies is largely based on average reflectance from the outcrop face. This chapter examines whether the reflectance spectra of four lithofacies types described in an outcrop transect of Pryor Quarry are unique, and can be differentiated proving the viability of sUAS based partial-SWIR hyperspectral imaging for documenting the mineralogy of outcrops.

2. Geologic Background and Study Area

The Meramecian-Chesterian Series in northeastern Oklahoma reflects a subtropical climate that produced a mixed carbonate-siliciclastic ramp complex on the southern margin of the Burlington Shelf, a broad, shallow carbonate factory that covered most of the midcontinent during the Mississippian (Gutschick and Sandberg, 1983). Shifting climate and the characteristically low relief bathymetry of the ramp system imparted strong, eustatically-controlled, cyclicity in these strata (Gutschick and Sandberg, 1983; Shelley, 2016). Similar deposits are thought to have developed along strike in a western direction into central and western Oklahoma. Although the provenance of the detrital, siliciclastic silt, which was abundant in the Meramecian series, is uncertain, previous workers have speculated an origin within regions of the Ozark uplift (Simms and Simms, 1995).

The Pryor Quarry, located on the western flank of the Ozark uplift in Mayes County, Oklahoma, is bounded to the south by the Arkoma Basin, to the west by the Nemaha uplift, and to the north by the Burlington shelf (Fig. 1). Previous work in Pryor Quarry by Godwin (2017) was conducted as part of a broader project focused on establishing a regional understanding of lithostratigraphy, sequence stratigraphy and biostratigraphy of Meramecian outcrops for the purposes of correlation to other outcrops and the subsurface of the southern midcontinent. In addition, Shelley (2016) examined three outcrop walls in a pit located in the southwestern portion of Pryor Quarry, where he described the lithostratigraphy and sequence stratigraphy of Meramecian strata.

3. Methods

3.1 Outcrop Description

Outcrop descriptions were taken from a single vertical outcrop transect in the southeast corner of D-pit at Pryor Quarry Oklahoma (Fig. 2). The outcrop was described by taking note of sedimentary structures, bedding thickness, and lithology at the decimeter scale, where possible. Heavy fracturing, presumably from blasting, ground water mineralization, plant debris, and mm-thick weathering rinds on the surface of the outcrop obscured some details of bed scale architecture from being thoroughly described. Outcrop descriptions of bedding thickness were supplemented using geometrically corrected outcrop models from sUAS-based photogrammetric images (Fig. 3).

3.2 Portable X-ray Fluorescence Analysis

pXRF geochemical analyses were collected using an Olympus Vanta M Series XRF Analyzer on each of 70 samples taken from a single vertical outcrop transect in the southeast corner of D-pit at Pryor Quarry Oklahoma. Outcrop samples were collected approximately every 0.3 m (1 ft). To account for instrument drift, Montana Soil Standard SRM 2711a was measured at the start and end of each day of sampling. If abundances of the primary elements present in the standard drifted from known laboratory values by more than 10%, the film over the instrument beam was cleaned, the settings were checked, and the process repeated until the instrument achieved results within an acceptable margin of error.

3.3 Laboratory Point Spectroscopy

An ASD Fieldspec 4 Spectroradiometer with a spectral range of 350-2500 nm and a spectral resolution of 1 nm was used to measure point spectroscopy data on both weathered (n=46) and unweathered (n=62) surfaces from the 70 total rock samples collected from the

outcrop transect. Some rock samples either did not possess a fresh surface or a representative weathered surface adequate for sampling. For the rock samples that were imaged, ten spectral measurements were taken at different points on the rock sample and averaged to avoid sampling error associated with imaging a non-representative portion of the sample. A single 250-watt halogen light was used to illuminate the surface of each sample prior to imaging.

3.4 sUAS-Based Photogrammetry

A DJI Mavic Pro was used to capture high resolution (20 megapixel) outcrop photographs of the quarry area and outcrop faces. Geometrically corrected orthophotos were constructed using Agisoft Metashape software.

3.5 sUAS-Based Hyperspectral Outcrop Imaging (900-1700nm)

A BaySpec OCI™-F Series push-broom hyperspectral sensor and minicomputer were mounted to a DJI Matrice 600 Pro Hexacopter using a DJI three axis Ronin Gimbal Stabilizer. Adjustments were made to the gimbal mount to orient the sensor to face the outcrop wall for facade scanning prior to takeoff. Subsequently flight plans were constructed using Universal Ground Control Software (UCGS). Flight path, speed, and orientation were specified and built into the flight plans. The design of each flight entailed flying the sUAS to the top of the outcrop making a horizontal pass across the outcrop face of length 20 m, followed by a downward vertical movement another horizontal pass and so on. Depending on the distance the sUAS flew from the face, it took fewer or greater passes to image the full outcrop. In this manner, the entirety of the outcrop of interest could be imaged at a high spatial resolution.

Two primary flight plans were used in this study. The first flight plan was programmed to fly 25 meters from the outcrop wall, at a horizontal scanning speed of 0.5 m/s for a total of 4 horizontal passes. The second flight plan was set to fly 15 meters from the outcrop wall at a

horizontal speed of 0.5 m/s for a total of 6 horizontal passes. Both plans were designed to start horizontal scans at the top of the outcrop and drop the appropriate vertical distance to fill the sensors field of view with a new portion of the outcrop not scanned in the last pass. The appropriate calculations were made for vertical drop distance between each pass by inputting sensors specifications into UCGS. After being designed in UCGS, software flight plans were uploaded to the DJI Matrice 600 prior to takeoff.

To control the sensor aboard the sUAS, a WiFi hotspot and VNC viewing software hosted from a field laptop were used to establish a remote connection between the sUAS mounted minicomputer controlling the sensor and the field laptop. Once a connection was established to the minicomputer, data capture was initiated prior to takeoff using the "Specgrabber" software. Because the remote connection between the field laptop and the sensor minicomputer could only be established with the sUAS on the ground, a timer was used in the "Specgrabber" software to delay the start of data capture by 30 seconds following takeoff. The additional 30 seconds before data capture was initiated allowing the sUAS to take off and travel to the start of the scanning area before data capture began. This prevented needless data from being collected on the minicomputer, which possessed limited hard drive space. Following the completion of its flight path, the sUAS returned to home, a remote connection was established with the minicomputer, and data capture was terminated.

4. Results

4.1. Outcrop Transect Description and pXRF Elemental Analysis

The outcrop transect described in this study is comprised of two formations with distinctive compositional and depositional characteristics: the basal Meramecian Pryor Creek Formation and the overlying Chesterian Hindsville Formation (Fig. 4). The Pryor Creek

Formation in this transect is described as a series of thick to thinly bedded, fine- to coarse-grained skeletal wackestones, packstones and grainstones overlain by interbedded argillaceous mudstones and siltstones with increased Si and Al content and minimal skeletal fragments (Fig. 4). The overlying Hindsville Formation possesses considerably less detrital content and is primarily comprised of coarse skeletal packestones and grainstones with few <0.5 m beds of argillaceous mudstone present in the bottom half of the formation. Bedding attitudes are nearly horizontal in Pryor Quarry. The geochemical distribution of the four lithofacies from the outcrop transect demonstrate that compositional differences are gradational in nature between lithofacies types (Fig. 5).

Lithofacies 1 Skeletal Packstone to Grainstone

Lithofacies 1 is a medium to dark gray, skeletal packstone to grainstone with cm-scale, bi-directional crossbedding. Mostly fragmental crinoids, echinoderms, and brachiopods are all abundant in this lithofacies. Although lithofacies 1 occurs most abundantly in the Hindsville Formation, several meters are observed in the Pryor Creek Formation as well. In the orthophoto of the vertical outcrop transect, lithofacies 1 is observed to be the most competent layer on the outcrop face and often protrudes over less competent layer of mudstone in lithofacies 3 (Fig. 4). Bedding thickness is variable from 1 cm to several m, although it is challenging to discern due to fracturing in the rock. Lithofacies 1 has an average Si, Ca, and Al content of 7%, 31%, and 2% respectively.

Lithofacies 2 Calcareous Mudstone to Wackestone

Lithofacies 2 is a light to medium gray, highly effervescent mudstone to wackestone that includes up to approximately 25% skeletal fragments. This lithofacies is slightly less competent in outcrop, when compared to lithofacies 1. Bedding features are primarily massive, but dm-scale

bedding and occasional burrowing does occur in muddier intervals of this lithofacies. The faunal assemblage of lithofacies 2 is composed of crinoid, echinoderm, and brachiopod remains. Lithofacies 2 has an average Si, Ca, and Al content of 14%, 22%, and 3% respectively.

Lithofacies 3 Mudstone

Lithofacies 3 stands out as a low competency, fissile to massive, medium to dark gray mudstone in outcrop. Lithofacies 3 is thinly bedded, rich in clay, and has interbeds of quartz silt throughout. Rare <0.1 m (0.3 ft) lag deposits rich in brachiopod fragments do occur, although typically only where this lithofacies overlies packstones and grainstones of lithofacies 1. This lithofacies occurs primarily around the contact between the Meramecian and Chesterian strata. Lithofacies 3 has an average Si, Ca, and Al content of 18%, 17%, and 4% respectively.

Lithofacies 4 Quartz Siltstone

Lithofacies 4 is a partially calcite-cemented, quartz siltstone that is mildly effervescent. Inclined to planar bedding is common and the bioturbation index is a 2. Lithofacies 4 is light gray in outcrop and not visually distinguishable from lithofacies 1 and 2. This lithofacies only occurs in the uppermost member of the Meramecian Pryor Creek Formation. Lithofacies 4 has an average Si, Ca, and Al content of 19%, 12%, and 4% respectively.

4.2. Laboratory Point Spectroscopy

Results of the reflectance spectroscopy data are subdivided by lithofacies and by surface type (i.e., unweathered or weathered) in Fig. 6. Absorption features are observed in each lithofacies, including H_2O and Al-OH around 1900 nm and 2200 nm signaling the presence of clay as well as CO_3 associated with calcite at approximately 2340 nm and 2500 nm (Fig. 6). Physical and chemical weathering influences the reflectance spectra of each lithofacies in the partial-SWIR range (900-1700 nm). Weathered samples of each lithofacies display lower

reflectance in the visible portion of the spectrum (380-740 nm) than do unweathered samples (Fig. 6). However weathered samples of lithofacies 1, 3, and 4 generate higher reflectance in wavelengths greater than 1000 nm the exception being lithofacies 2 which possesses roughly equal reflectance on weathered samples above 1500 nm.

10^{th} and 90^{th} percentiles for both unweathered and weathered samples demonstrate that the spread of each lithofacies reflectance spectra in the partial-SWIR overlaps significantly between some lithofacies (Fig. 7). In unweathered samples, lithofacies 1 and 2 have very similar average reflectance spectra, whereas lithofacies 4 is slightly less reflective and lithofacies 3 is significantly more reflective sharing only minimal percentile overlap with other lithofacies. In weathered samples, lithofacies 2 and 4 have very similar average reflectance spectra, whereas lithofacies 1 and 3 have higher average reflectance spectra with only some overlap occurring in the 10^{th} to 90^{th} percentile range (Fig. 7). In general, less overlap occurs between percentile intervals for the weathered samples than the unweathered samples. Apart from lithofacies 3, individual lithofacies do not appear to possess systematically distinctive reflectance spectra in the partial-SWIR range for either unweathered or weathered samples (Fig. 7).

5. Discussion

5.1. Depositional Environmental Interpretation

Bi-directional cross bedding, abundant skeletal grains, and high Ca content in lithofacies 1 suggest deposition in a shallow water, inner ramp setting, an interpretation that agrees with previous work by Shelley (2016). Lithofacies 2 has a higher proportion of carbonate mud, more Si, fewer skeletal fragments or sedimentary structures than lithofacies 1, suggesting deposition in a mid-ramp setting, which agrees with previous depositional interpretations by Shelley (2016) and Godwin (2017) of similar rock types. Lithofacies 3 and 4 likely represent outer ramp

deposits, where finer grained fractions of detrital quartz silt and clay accompanied by some lime mud fell out of suspension basinward of the higher energy, bioclastic deposition in inner ramp settings. We speculate that siliciclastic detrital content increases with water depth as a function of grain size. Previous work by Shelley (2016) identifies higher reservoir quality in distally deposited lithofacies with increasing clay and quartz silt content, where clay prevents the nucleation of porosity occluding calcite cements.

5.2. Laboratory Point Spectroscopy and Viability of sUAS-Based Partial-SWIR Hyperspectral Imaging for Outcrop Characterization

The effects of physical and chemical weathering on rock sample surfaces, and by extension outcrop surfaces, modifies the reflectance spectra of the underlying lithologies. Weathered samples of each lithofacies type display lower reflectance in the visible portion of the spectrum (380-740 nm), which is expected as weathered samples typically possess a duller, less reflective surface than fresh unweathered samples do when examined with the naked eye. At approximately 1000 nm, the average reflectance of weathered samples of lithofacies 1, 3, and 4 exceeds that of unweathered samples. For lithofacies 2, no difference in average reflectance spectra exists between unweathered and weathered samples, which may indicate that the spectral characteristics of lithofacies 2 are less dependent on weathering processes. Lithofacies 1 exhibited the most pronounced change, with unweathered surfaces having notably higher reflectance than weathered samples, possibly reflecting the tendency for coarser-grained lithologies to develop thick weathering rinds (Fig. 6).

The effects of weathering on the underlying lithology of the outcrop should be considered when planning a remote sensing survey, as the point spectroscopy data suggest that reflectance spectra in the partial-SWIR can be significantly altered by processes of weathering (Fig. 6).

However, weathering appears to exaggerate differences in lithofacies types rather than suppressing them, which ultimately makes classifying weathered outcrops more ideal than unweathered outcrops (Fig. 7). Ideally, any outcrop under study will possess an invariant degree of weathering across its face. Alternatively, full-SWIR data may be less susceptible to the effects of surficial weathering, as the magnitude and position of absorption features do not appear to be significantly influenced by weathering processes (Fig. 7).

A comparative examination of each weathered lithofacies suggests that lithofacies 3 is the most easily distinguished on the basis of its high reflectivity across the spectral range. Lithofacies 2 and 4 are nearly indistinguishable from reflectance spectra alone (Fig. 7). Lithofacies 1 is transitional between the others and is thus, characterized by a certain degree of overlap in spectral frequencies (Fig. 7). Among unweathered samples, lithofacies 1 (skeletal packstones and grainstones) and lithofacies 2 (wackestones) possess similar average reflectance and percentile ranges, which is consistent with these lithofacies types being both limestones, and thus dominated by the mineral calcite. Among weathered samples lithofacies 2 and 4 possess similar average reflectance and percentile ranges.

Because differences between lithofacies in the partial-SWIR range are predominantly a function of spectral reflectance (Fig. 7), partial-SWIR data collected from natural outcrops may be susceptible to issues related to inconsistent solar radiation across the face of the outcrop. The amount of solar energy reflected by a given area on an outcrop depends on the amount of energy incident on that area, which in turn depends on the angle at which the light energy strikes the surface of the outcrop. This is presumed to be relatively constant in a laboratory setting, as was used for the collection of point spectroscopy data, where an artificial light source maintains a constant angle of incidence on a prepared sample with a smooth surface. In this way the

underlying properties of a material can be studied, to the extent that variations in the angle at which energy strikes the scene is not influenced by microtopography of the sample or a moving light source. In the field, however, changes in the angle of solar incidence throughout the day may have an effect on the results, if the data are not collected within a short span of time. Seasonal shifts also influence the angle of incident solar radiation, potentially making it challenging to compare datasets collected at different times of the year. Finally, the uneven surface of natural outcrops is likely to result in uneven solar intensity, including harsh shadows. Because differences in lithologies in the partial-SWIR range are primarily a function of spectral reflectance, natural variation in rock surface topography may obfuscate the underlying mineralogic controls on partial-SWIR data. These results suggest that partial-SWIR analysis of outcrop exposures is most likely to be successful when 1) the outcrop face is weathered and if weathering intensity is invariant across the outcrop face, 2) the data collection occurs over a sufficiently short timespan such that the angle of incident solar radiation is approximately invariant, and 3) the outcrop lacks significant topographic relief and roughness that may cause shadowing.

6. Conclusions

Conventional descriptive techniques paired with pXRF and point spectroscopy were used to document four predominant lithofacies types in an Upper Mississippian outcrop in Pryor Quarry Oklahoma. Lithofacies types include Ca-rich packstones and grainstones likely deposited in shallow high energy environments to argillaceous quartz mudstones and siltstones with high proportions of Si and Al, likely deposited in a distal ramp environment. Point spectroscopy (350-2500 nm) data suggest that the products of physical and chemical weathering can strongly influence the spectral reflectivity of rock outcrops in the partial-SWIR. Additionally, weathered

samples appear to possess more distinctive average reflectance spectra than unweathered samples. Of the four lithofacies described and sampled in Pryor Quarry only lithofacies 3 possesses distinctive reflectance spectra in the partial-SWIR. Furthermore, a discussion of illumination geometry highlights the serious technical issues associated with normalizing incident intensity values in a field setting for outcrop imaging. Considering this, care must be taken in implementing sUAS-based partial-SWIR hyperspectral imaging of outcrop faces to minimize potential limitations of this approach.

References

Burchette, T.P., and Wright, V.P., 1992, Carbonate ramp depositional systems: Sedimentary Geology, v. 79, p. 3–57, doi:10.1016/0037-0738(92)90003-A.

Coffey, W., 2001, Lithostratigraphy and Porosity Characterization of the Sycamore Formation (Mississippian), and it's Relationship to Reservoir Performance, Carter-Knox Field, Grady and Stephens county, Oklahoma: , p. 9–17, http://archives.datapages.com/data/ocgs/data/052/052001/0009.htm.

Cooper, C.D., and Mustard, J.F., 1999, Effects of Very Fine Particle Size on Reflectance Spectra of Smectite and Palagonitic Soil: Icarus, v. 142, p. 557–570, doi:10.1006/icar.1999.6221.

Godwin, C.J., 2017, Lithostratigraphy and Conodont Biostratigraphy of the Upper Boone group and Mayes Group in the Southwestern Ozarks of Oklahoma, Missouri, Kansas, and Arkansas. PhD. thesis, Oklahoma State University, Stillwater, Oklahoma.

Gutschick, R.C., and Sandberg, C.A., 1983, Mississippian continental margins of the conterminous United States.: Society for Sedimentary Geology, p. 79–96.

Miller, J., 2018, Regional Stratigraphy and Organic Richness of the Mississiippian Meramec and Associated Strata, Anadarko Basin, Central Oklahoma, doi:10.1051/matecconf/201712107005.

Mohamed, E.S., Saleh, A.M., Belal, A.B., and Gad, A.A., 2018, Application of near-infrared reflectance for quantitative assessment of soil properties: Egyptian Journal of Remote Sensing and Space Science, v. 21, p. 1–14, doi:10.1016/j.ejrs.2017.02.001.

Nieminski, N.M., and Graham, S.A., 2017, Modeling Stratigraphic Architecture Using Small Unmanned Aerial Vehicles and Photogrammetry: Examples From the Miocene East Coast Basin, New Zealand: Journal of Sedimentary Research, v. 87, p. 126–132, doi:10.2110/jsr.2017.5.

Okyay, Ü., Khan, S.D., Lakshmikantha, M.R., and Sarmiento, S., 2016, Ground-based hyperspectral image analysis of the lower Mississippian (Osagean) reeds spring formation rocks in southwestern Missouri: Remote Sensing, v. 8, doi:10.3390/rs8121018.

Price, B.J., Pollack, A.C., Lamb, A.P., Peryam, T.C., and Anderson, J.R., 2020, Depositional interpretation and sequence stratigraphic control on reservoir quality and distribution in the Meramecian STACK play Depositional interpretation and sequence stratigraphic control on reservoir quality and 1 distribution in the Meramecian STAC: AAPG Bulletin, v. 104, p. 357–386, doi:10.1306/04301917411.

Shelley, S.A., 2016, Outcrop-Based Sequence Stratigraphy and Reservoir Characterization of an Upper Mississippian Mixed Carbonate- Siliciclastic Ramp, Mayes County, Oklahoma. M.S. thesis, Oklahoma State University, Stillwater, Oklahoma, 75 p.

Simms, J., and Simms, F., 1995, The Geology of the Southwestern Ozark Uplift.

Stright, L., Stewart, J., Campion, K., and Graham, S., 2014, Geologic and seismic modeling of a coarse-grained deep-water channel reservoir analog (Black's Beach, La Jolla, California): AAPG Bulletin, v. 98, p. 695–728, doi:10.1306/09121312211.

Sun, L., Khan, S.D., Sarmiento, S., Lakshmikantha, M.R., and Zhou, H., 2017, Ground-based hyperspectral imaging and terrestrial laser scanning for fracture characterization in the Mississippian Boone Formation: International Journal of Applied Earth Observation and Geoinformation, v. 63, p. 222–233, doi:10.1016/j.jag.2017.08.008.

Sun, L., Khan, S., and Shabestari, P., 2019, Integrated hyperspectral and geochemical study of sediment-hosted disseminated gold at the Goldstrike District, Utah: Remote Sensing, v. 11, doi:10.3390/rs11171987.

Turmelle, T.J., 1982, Lithostratigraphy and Deposistional Environments of the Mayes Formation (Mississippian) in Adair County, Oklahoma. M.S. thesis, University of Oklahoma, Norman, Oklahoma.

van der Meer, F., 2004, Analysis of spectral absorption features in hyperspectral imagery: International Journal of Applied Earth Observation and Geoinformation, v. 5, p. 55–68, doi:10.1016/j.jag.2003.09.001.

Figures

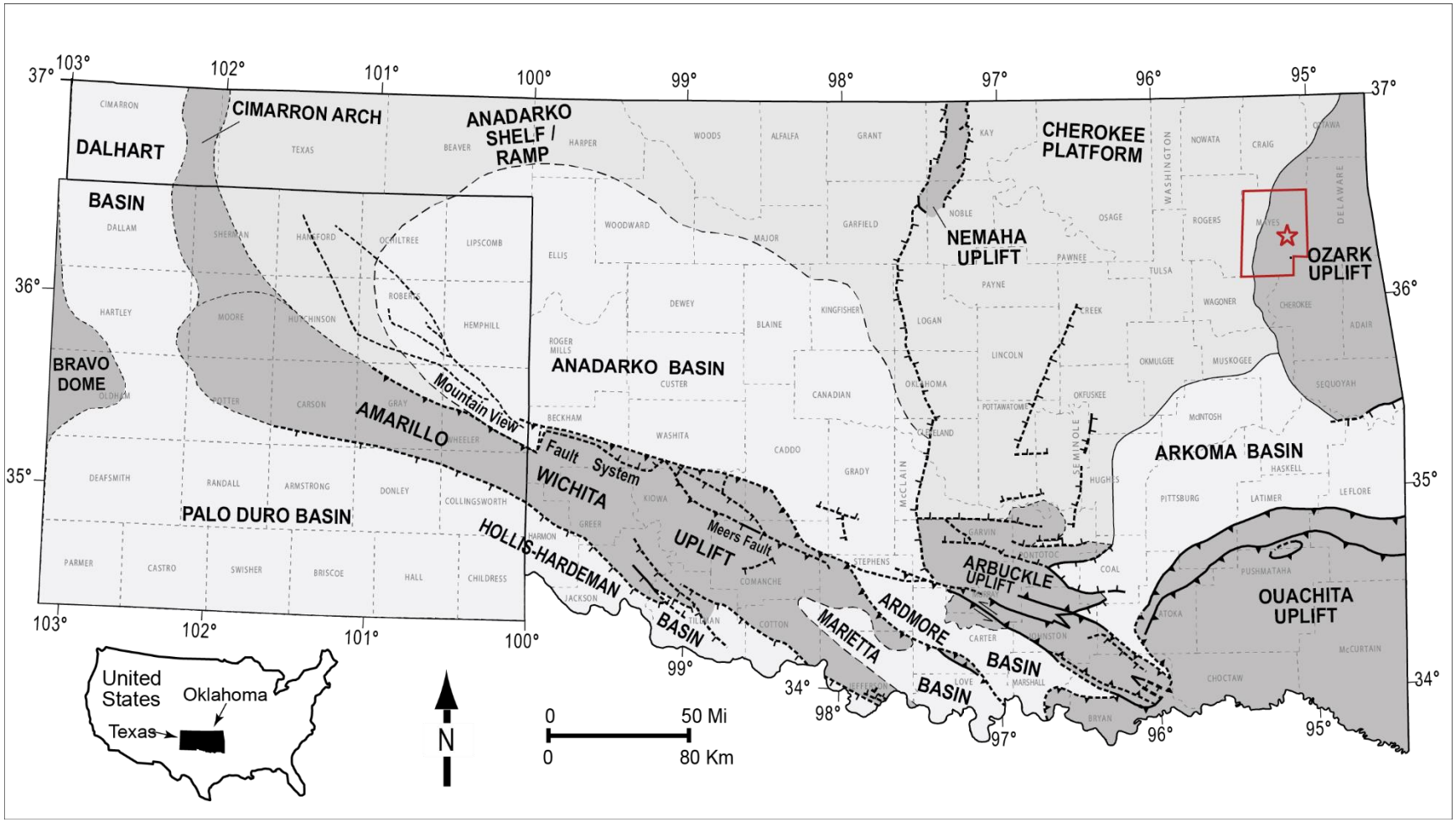

Figure 1. Structural provinces of Oklahoma. Mayes County, outlined in red, Pryor Quarry denoted by the red star. Adapted from Miller, 2018.

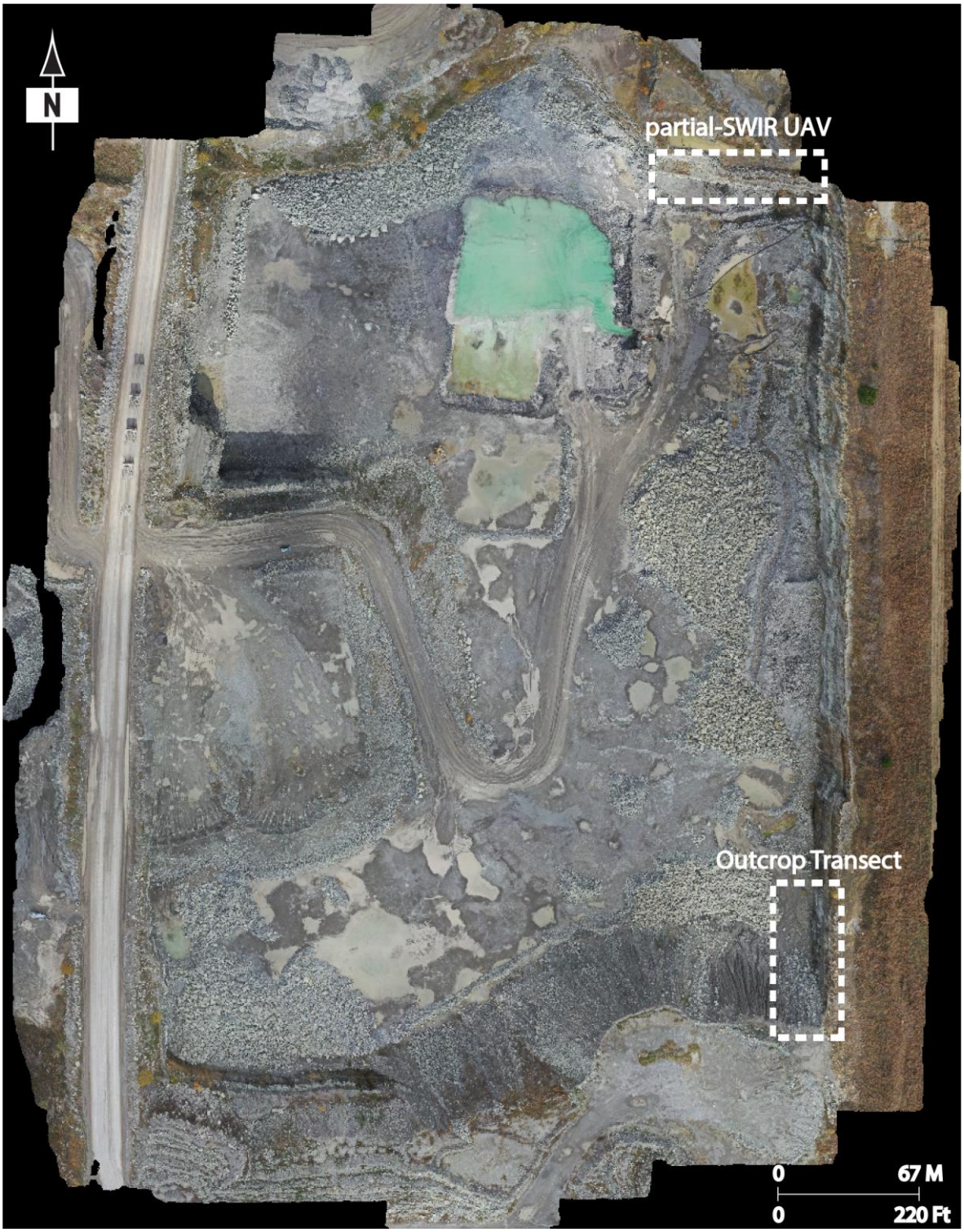

Figure 2. Aerial orthophoto of D-pit at Pryor Quarry. Outcrops in the southeast corner of D-pit were described in this study. sUAS-based hyperspectral imaging was conducted on the north wall outcrop.

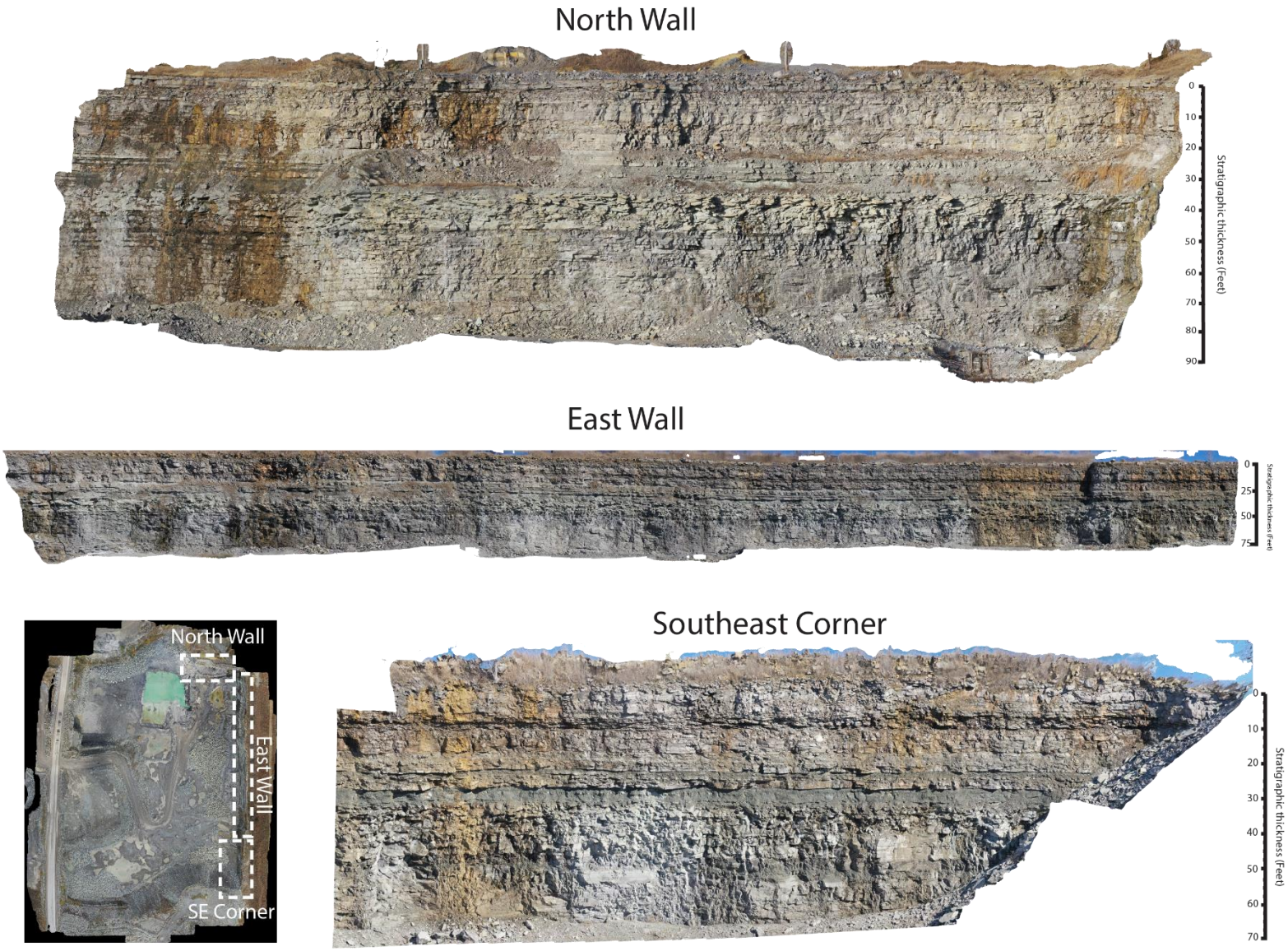

Figure 3. Composite orthophotos of the north and east wall, and southeast corner of D-pit at Pryor Quarry.

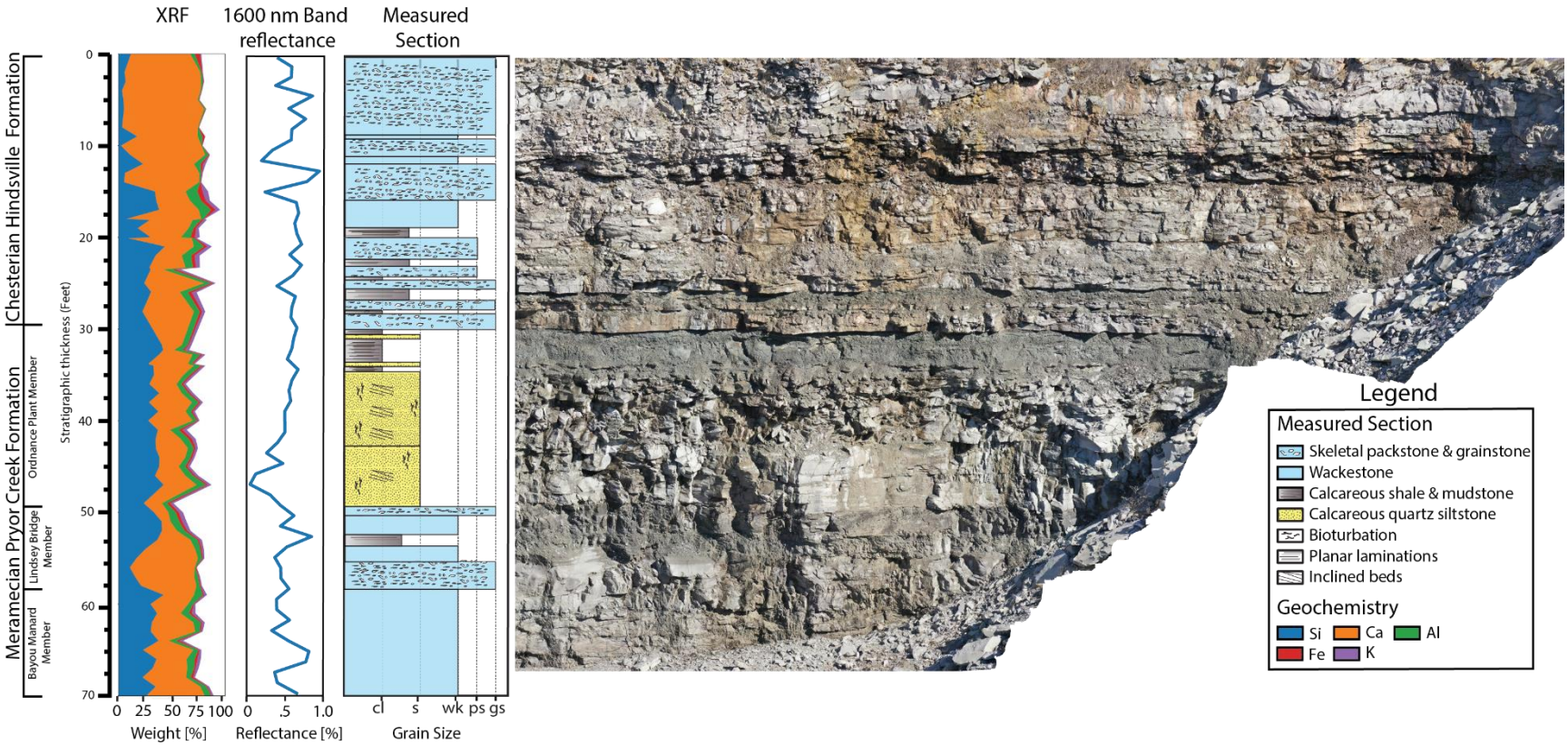

Figure 4. Depth referenced stratigraphic column, pXRF data, point spectrocopy data from band 1600 nm, and orthophoto for the southeast corner outcrop of D-pit, Pryor Quarry. Abbreviations: cl-clay; gs-grainstone; ps-packstone; s-silt; ws-wackestone.

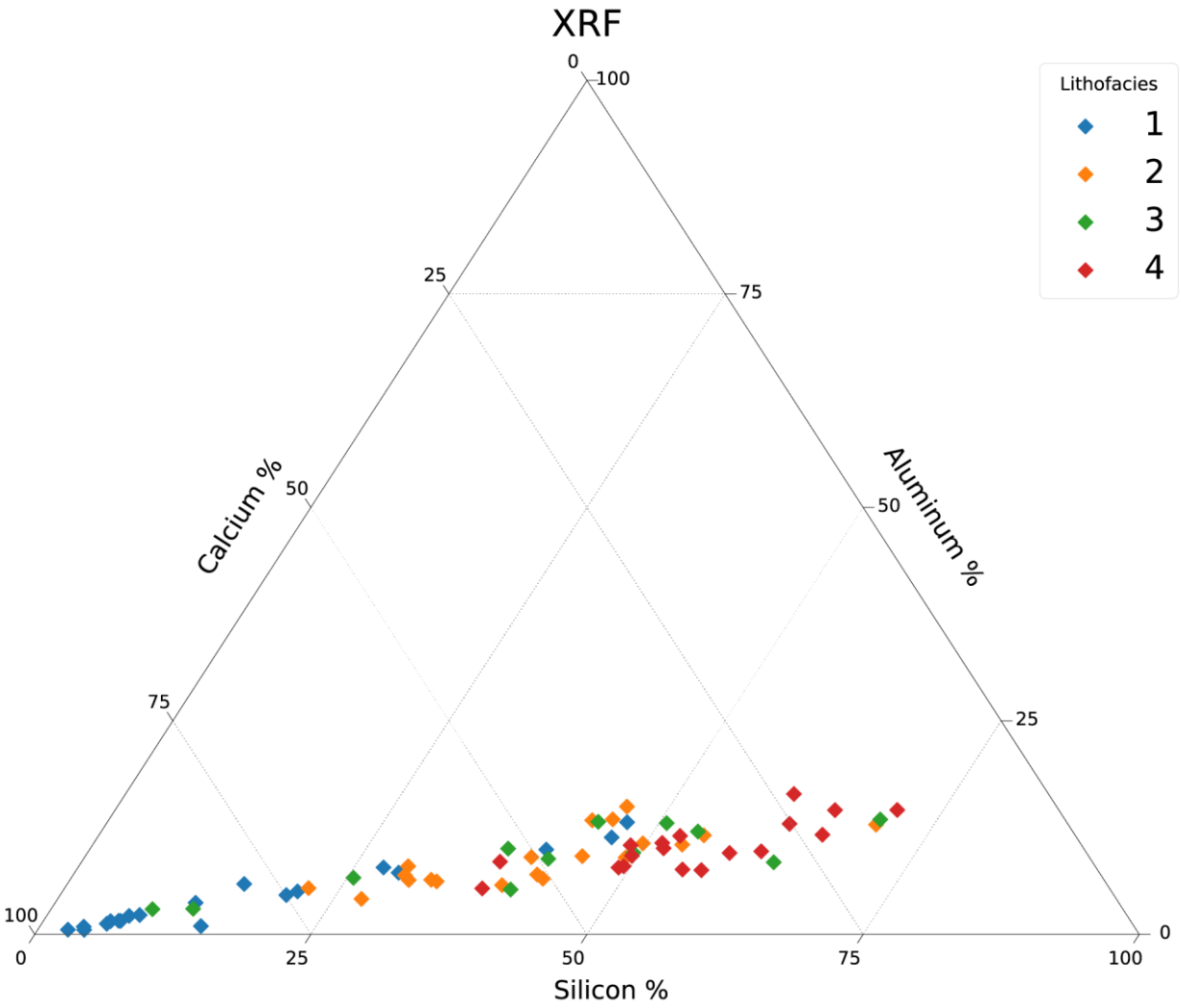

Figure 5. pXRF results colored by lithofacies type.

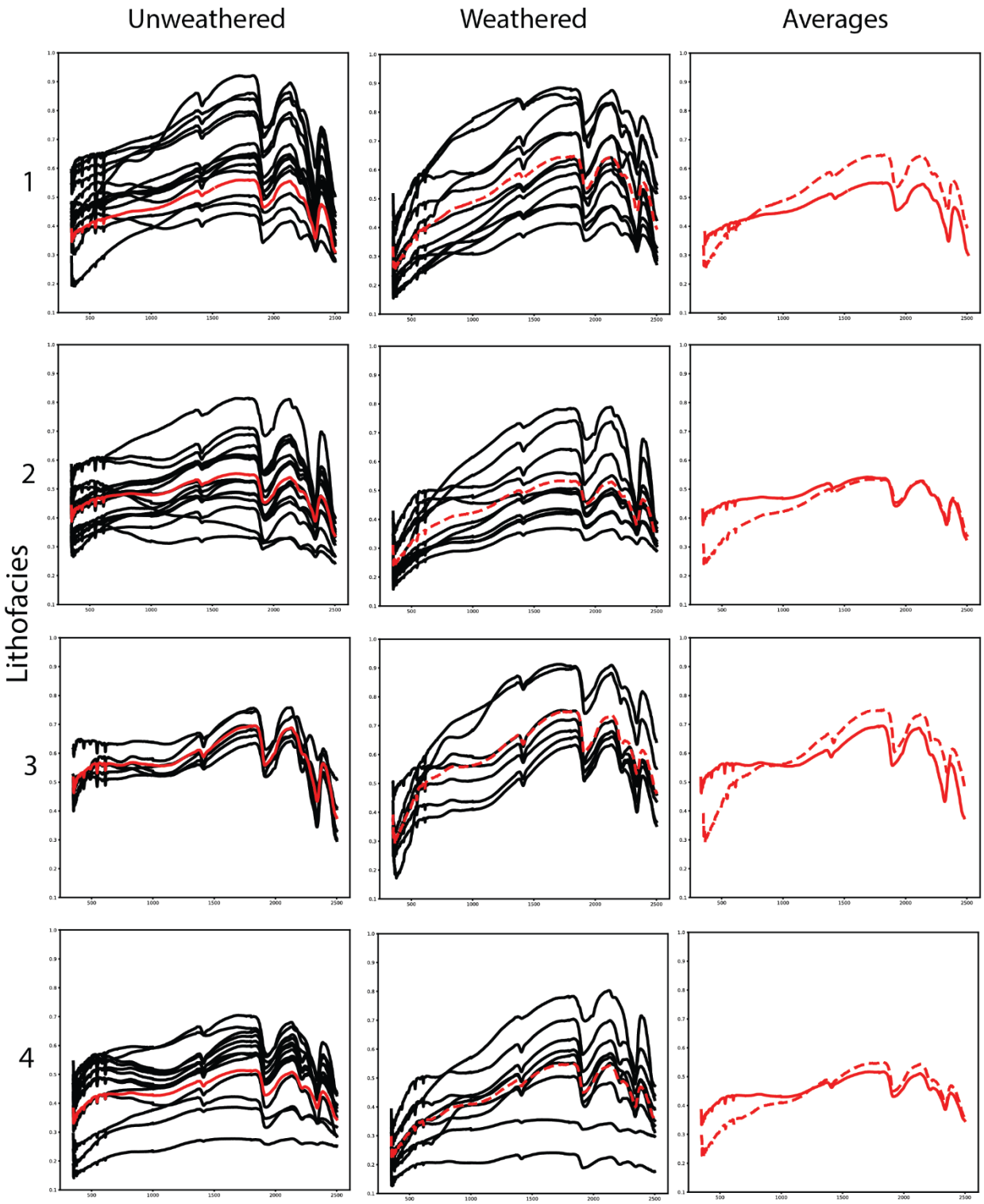

Figure 6. Full-SWIR spectral signatures by lithofacies type and weathering surface type. Solid red line denotes mean of unweathered samples, dashed red line indicates mean of weathered samples.

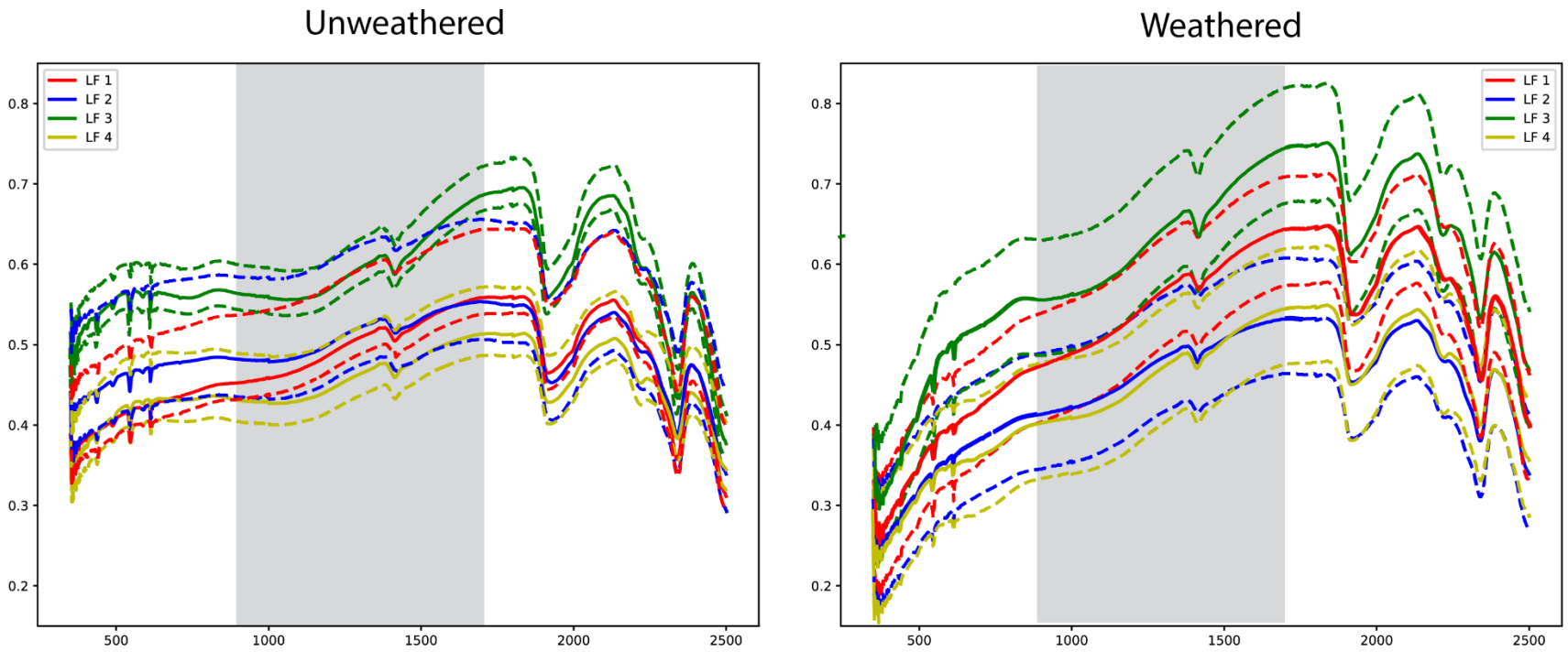

Figure 7. Solid colored line indicates Mean full-SWIR spectral signatures by lithofacies type and dashed colored lines demarcate 10th and 90th percentiles. Gray background denotes the range of partial-SWIR (900-1700 nm) data.

Chapter 4

Conclusions

This study presents an integrated analysis of hyperspectral, geochemical, and stratigraphic data for the purpose of characterizing the mineralogy and sedimentology of Upper Mississippian strata within the Anadarko Basin (Meramec Formation, STACK Play) and Ozark Uplift region (Pryor Creek Formation). Novel approaches to laboratory- and sUAS-based partial-SWIR hyperspectral imaging were developed for analysis of drill core and outcrop, respectively.

Chapter 2 focuses on analysis of two drill cores within Canadian and Dewey counties, of the STACK Play, Oklahoma. Both proximal and distal ramp environments are interpreted in core and include argillaceous quartz siltstones, calcareous quartz siltstones and sandstones, and to a lesser extent grainstones. Lab-based partial-SWIR hyperspectral imaging was successfully employed to document primary mineralogic variability in both cores. Findings revealed a dual endmember scheme where pixels abundant in clay and quartz were associated with low partial-SWIR reflectance values and pixels abundant in calcite were strongly correlated with high partial-SWIR reflectance values. The relationship between reflectance and mineralogy was leveraged to examine stratigraphic cyclicity at multiple scales in the core. Up to 5 orders of stratigraphic cyclicity were interpreted from the hyperspectral data in conjunction with core descriptions, geochemical, and mineralogic data. The mm-scale spatial resolution of the hyperspectral data revealed 4th and 5th order cyclicity associated with processes that exist well below the resolution of conventional well data. Core descriptions and interpretations of hyperspectral cyclicity corroborate the findings of previous workers that coarsening upward cycles observed in the Meramec Formation, termed 3rd order cyclicity in this study, are the product of a series of prograding clinoforms deposited in a ramp setting. These 3rd order cycles

are superimposed on a sequence of 2nd order cycles of sea level rise and fall that are ultimately superimposed on an overall period of sea level rise (1st order).

Chapter 3 focuses on describing and analyzing an outcrop transect in Pryor Quarry, Mayes County, northeastern Oklahoma using conventional descriptive, geochemical, and spectroscopy methods. Lithofacies types described in Pryor Quarry include Ca-rich packstones and grainstones likely deposited in shallow high energy environments to argillaceous quartz mudstones and siltstones with high proportions of Si and Al likely deposited in a distal ramp environment. Point spectroscopy data collected from outcrop samples suggest that physical and chemical weathering can strongly influence the spectral reflectivity of rock in the VNIR and full-SWIR ranges (350-2500 nm). The four lithofacies defined in Pryor Quarry are characterized by variable differences in the partial-SWIR spectral range, with lithofacies 3 being the most distinct. These spectral differences are augmented by physical and chemical weathering and may be potentially leveraged to map the distribution of certain lithofacies at the outcrop scale using sUAS-based partial-SWIR hyperspectral imaging. However, the ability to control and normalize incident light intensity in a field setting may present a challenge to partial-SWIR data that depends on differences in spectral reflectivity rather than absorption feature analysis. Specifically, daily and seasonal changes in the angle of incident solar energy and inherent topography of outcrop faces may result in changes to measured spectral reflectance that are not related to outcrop lithology or mineralogy. These results suggest that partial-SWIR data may be most applicable to outcrop characterization when (1) the outcrop face is weathered and if weathering intensity is invariant across the outcrop face, (2) the data collection occurs over a sufficiently short timespan such that the angle of incident solar radiation is approximately

invariant, and (3) the outcrop lacks significant topographic relief and roughness that may cause shadowing.